Plasma membrane accessible cholesterol is regulated by ACC1 and lipid droplets

Kalani M. Wijesinghe[1], Chai-wan Kim[2], Emily O. Schad[1], Shuo Li[1], Summer Chen[1], Erin Takeshima[1], Chandni B. Khandwala[1], Desiree Tillo[3], Andres M. Lebensohn[4], James A. Olzmann[5], Rajat Rohatgi[1], Maia Kinnebrew[1,6]

[1] Departments of Biochemistry and Medicine, Stanford University School of Medicine, Stanford, CA 94305, USA
[2] Center for Human Nutrition and Department of Internal Medicine, University of Texas Southwestern Medical Center, Dallas, TX 75390-9046, USA
[3] Center for Cancer Research Genomics Core, National Cancer Institute, National Institutes of Health, NIH, Building 41, RM D701, Bethesda, MD 20892, USA.
[4] Laboratory of Cellular and Molecular Biology, Center for Cancer Research, National Cancer Institute, National Institutes of Health, NIH, Building 37, RM 2056C, Bethesda, MD 20892, USA.
[5] Department of Molecular and Cell Biology, University of California at Berkeley, Berkeley, CA, USA and Department of Nutritional Sciences and Toxicology, University of California at Berkeley, Berkeley, CA 94720, USA.
[6] Lead contact

Abstract

Proper maintenance of plasma membrane (PM) cholesterol is essential for diverse processes ranging from animal development to pathogen evasion. Despite decades of study, the mechanisms governing cellular cholesterol regulation are incomplete. Using genome-wide screens we find that ACC1, the rate-limiting enzyme in fatty acid biosynthesis, regulates PM cholesterol transport. ACC1 loss causes a ~10-fold increase in PM accessible cholesterol in cells and mice. Mechanistically, we find that ACC1 regulates lipid droplet (LD) catabolism, and LDs are intimately tied to PM accessible cholesterol levels since reductions or elevations in their numbers block or promote cholesterol trafficking, respectively. Furthermore, LDs are required for cholesterol trafficking induced by 25-hydroxycholesterol, a modulator of inflammation and an interferon-stimulated second messenger that protects cells from pathogen invasion. This work identifies an unrecognized role for ACC1 and LDs in cholesterol regulation, which has implications for diseases where LD numbers are altered, from metabolic syndromes to neurodegeneration.

Keywords: Cholesterol, accessible cholesterol, lipid droplet, plasma membrane, membrane trafficking, ACC1, ATGL, SREBP2, ACAT1 and ACAT2, AMPK, 25-hydroxycholesterol, triacylglycerol, cholesterol esters

Introduction

Cholesterol is a vastly important molecule: it makes up 40% of all lipids in the plasma membrane (PM) through the coordinated effort of nearly 100 proteins that regulate its

synthesis, transport and metabolism[1,2]. While being vital for cell and organismal health, it is also linked to numerous human diseases, including cardiovascular disease, metabolic syndrome, cancer and neurodegeneration. Despite a rich history of investigation dating to the 1700s and multiple Nobel prizes awarded to its study, we lack a complete understanding of how cholesterol is regulated[3]. For example, only in the last 15 years has a pivotal concept come to light: while the majority of cholesterol plays structural roles in the PM, ~2% of PM cholesterol has high chemical activity[4–7]. This pool of cholesterol, often referred to as *active* or *accessible* cholesterol, can dynamically bind to proteins and drive cell signaling events. The complete importance of accessible cholesterol in vivo is unknown, but thus far it has been shown to control de novo cholesterol synthesis, viral and bacterial pathogenesis, and the Hedgehog signaling pathway[8–13]. We hypothesize that significant breakthroughs related to the study of cholesterol in human diseases have been obscured because the majority of cholesterol research (99.98% of published articles) did not measure the accessible cholesterol pool. This study seeks to redefine our understanding of cholesterol by investigating this understudied yet functionally essential accessible cholesterol pool.

Accessible cholesterol is continually transported from the PM to the Endoplasmic Reticulum (ER) where its levels are sensed to control de novo cholesterol synthesis. When ER cholesterol is high, SCAP and SREBP2 are retained in the ER and cholesterol synthesis is blocked. When ER cholesterol is low, SCAP escorts SREBP2 to the Golgi where it is proteolytically cleaved into a transcriptionally active fragment that drives the expression of cholesterol biosynthesis genes[12,14–17]. A long-standing mystery is how changes in PM accessible cholesterol are conveyed to the cholesterol-sensing machinery in the ER. Additionally, are there proteins that sense and control the amount of PM accessible cholesterol directly?

The high accessible cholesterol content of vertebrate PMs has been exploited by both bacterial and viral pathogens for their entry into cells[10,13,18,19]. To counteract this, the immune system has evolved a mechanism to evade pathogens where PM accessible cholesterol levels are rapidly depleted. Interferon gamma signaling induces the expression of the enzyme cholesterol 25-hydroxylase (CH25H), which converts cholesterol to 25-hydroxycholesterol (25HC). 25HC diffuses across the cell membrane to surrounding cells, triggering rapid (~1-6 hours) PM cholesterol depletion by allosterically activating the ER localized proteins ACAT1 and ACAT2 (genes *SOAT1* and *SOAT2*). ACAT1/2 esterify cellular cholesterol, which is then stored in lipid droplets[20–22]. 25HC also reduces PM cholesterol on longer timescales that require the activation of transcriptional programs: 25HC elevates the expression of ABC transporters by activating LXR and it also activates INSIG to block new cholesterol synthesis[23–27]. How cholesterol is transported out of the PM in response to 25HC is unknown.

GRAMD1B is known to regulate accessible cholesterol-specific trafficking from the PM to the ER; it localizes in the ER and moves cholesterol down its concentration gradient at PM-ER contact sites[28–31]. Knockout of GRAMD1B (and triple knockout of GRAMD1A, GRAMD1B and GRAMD1C) does not affect cell viability, demonstrating that additional pathways for cholesterol transport out of the PM must exist. A subset of cytoplasmically localized START-domain containing proteins (StarD4, StarD5, and StarD6) have also been shown to bind cholesterol and control its intracellular trafficking; their relative contribution to PM cholesterol homeostasis has not been systematically investigated[32,33]. Finally, cholesterol can be internalized from the PM through vesicular transport, although there is no known endocytic pathway dedicated

specifically to maintaining cholesterol homeostasis[34–37]. In summary, we lack a complete picture of how accessible cholesterol is regulated in cells, which obscures our understanding of its function for cell and organismal physiology. We thus set out to solve this foundational mystery using an unbiased genetic screen to identify new genes controlling PM accessible cholesterol homeostasis. From here forward in this manuscript, unless specifically stated otherwise, any reference to cholesterol refers to accessible cholesterol.

Results

Random-insertion mutagenesis screens identify new cholesterol regulatory genes.

To test the known pathway of PM to ER cholesterol transport, we knocked out GRAMD1A, GRAMD1B and GRAMD1C (*GRAMD1A/B/C* TKO) in human haploid HAP1 cells (**Extended data Fig. 1a**)[28–31]. *GRAMD1A/B/C* TKO cells showed 1.2-fold elevated PM cholesterol, consistent with a defect in cholesterol trafficking out of the PM (**Fig. 1a**). However, when treated with 25HC, cholesterol was depleted from the PM with similar kinetics to wild-type (WT) cells (**Fig. 1b**). These results were indistinguishable to GRAMD1B single KO cells (**Extended data Fig. 1b-d**). 25HC can also reduce PM cholesterol levels by activating LXR and increasing the expression of ABC transporters that export cholesterol from the cell[26]. Overnight treatment with an LXR inhibitor strongly reduced ABCA1 transcript levels and slightly elevated PM cholesterol levels; however, it did not block PM cholesterol depletion induced by 25HC (**Fig. 1c**, **d and Extended data Fig. 1e-g**). These data demonstrate that when cells are stimulated with 25HC, cholesterol can exit the PM in a GRAMD1A/B/C- and LXR-independent manner. This raises the question: how does cholesterol exit the PM in response to 25HC (**Fig. 1e**)?

To find genes that regulate PM cholesterol, we devised a new genome-wide screening strategy. We reasoned that strong regulators of cellular cholesterol are likely to be required for cell viability, and therefore avoided CRISPR knockout screening. Instead, we used random-insertion mutagenesis to generate a library of ~100 million cells in the human haploid HAP1 cell line. This mutational strategy can generate hypomorphic alleles by truncating proteins or by reducing the transcriptional output of genes. Next, we stained live cells at the outer leaflet of the PM with the accessible cholesterol binding protein ALOD4 fused to mNeonGreen (mNG-ALOD4) to enrich cells whose cholesterol levels were altered (**Fig. 1f**) [38,39]. Using this strategy, we performed two screens probing distinct biological processes. We first treated cells with the NPC1 inhibitor U18666A for 20 hours, which reduces PM cholesterol by blocking low density lipoprotein (LDL)-derived cholesterol export from lysosomes. We then sorted for cells with the top 10% of mNG-ALOD4 fluorescence to identify mutants that rescue PM cholesterol in the absence of NPC1 function. In a second screen, we treated cells with 25HC for 6 hours and then sorted for cells with the top 10% of mNG-ALOD4 fluorescence to identify mutants in which cholesterol transport in response to 25HC was blocked. Strikingly, both screens identified ACC1 (*ACACA* gene) as the top hit by a large margin (**Fig. 1g**, **h**). ACC1 has been the subject of extensive research due to its role in human diseases, but it has not been linked to cholesterol regulation in cells; this motivated us to decipher this mystery.

ACC1 catalyzes the rate limiting step in fatty acid biosynthesis, converting acetyl-CoA into malonyl-CoA, which is then elongated by fatty acid synthase (FASN) to produce long-chain saturated fatty acids[40]. Interestingly, the majority of ACC1 insertions enriched in the screens

129

Fig. 1: Random insertion mutagenesis screens identify new cholesterol regulatory genes.

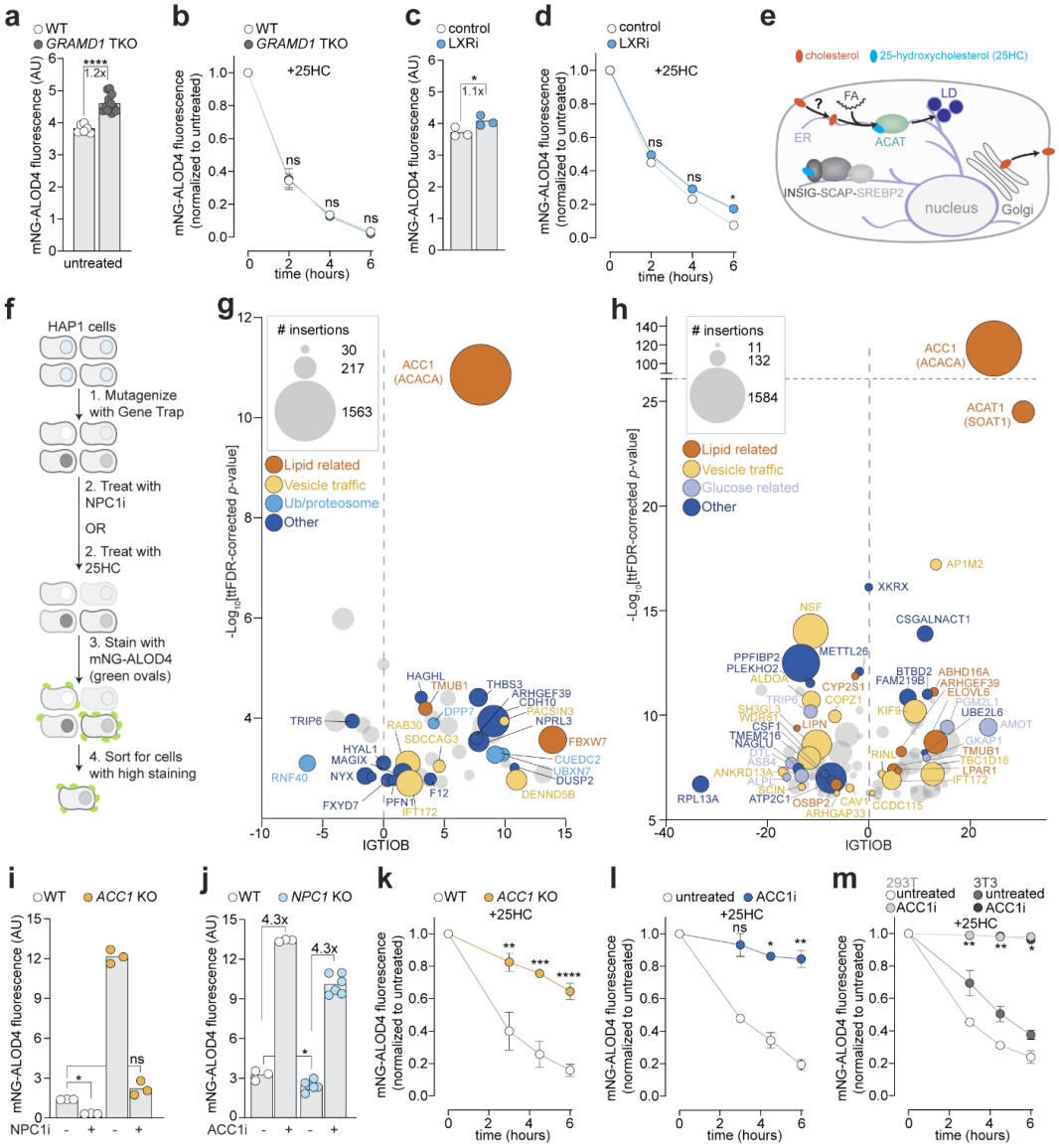

a-d, Plasma membrane (PM) cholesterol was measured by mNeonGreen-ALOD4 (mNG-ALOD4) staining followed by flow cytometry. Wild type (WT) HAP1 cells are compared to GRAMD1A, GRAMD1B, and GRAMD1C triple knockout HAP1 cells (*GRAMD1* TKO) either left untreated (**a**) or treated with 4 μM 25-hydroxycholesterol (25HC) for the times indicated (**b**). WT cells were treated with or without LXR inhibitor (LXRi; 1 μM GSK2033) for 16 hrs in 5% FBS and either left untreated (**c**) or treated with 25HC for the times indicated (**d**). **e**, Schematic showing cholesterol trafficking from the PM to the ER membrane where it binds to proteins including SCAP and ACAT1 or ACAT2 (ACAT). ACAT esterifies cholesterol with a fatty acid (FA), enabling it to be stored in lipid droplets (LD). Cholesterol is transported to the PM from the Golgi[89]. **f**, Schematic of genetic screening pipelines. The mutant cell library was treated with either of NPC1i (1 μM U18666A) for 20 hrs or 4 μM 25HC for 6 hrs and then cells were stained with mNG-ALOD4. The top 10% of mNG-ALOD4 fluorescent cells were isolated for sequencing. g,h, Screen results showing enriched genes with an FDR-corrected *p*-value of less than 2E-4 for cells treated with NPC1i (**g**) or 25HC (**h**). IGTIOB is a measure of the inactivating potential of the mapped insertions, and circle size shows the number of insertions for each gene. **i,j**, mNG-ALOD4 flow cytometry analysis of PM cholesterol in WT or *ACC1* KO HAP1 cells treated with or without 1 μM of NPC1i for 20 hrs (**i**) or WT and *NPC1* KO HAP1 cells treated with or without ACC1i (30 μM Firsocostat) for 16 hrs (**j**). **k-m**, Cells were left untreated (**k**) or treated for 16 hrs with 30 μM ACC1i and then treated with 4 μM 25HC for the times indicated (**l** and **m**). The amount of mNG-ALOD4 bound to the PM was measured by flow cytometry. Data is normalized to cells not treated with 25HC for each condition, and each circle is the mean of three biological replicates; error bars are the standard deviation. Statistical tests compare two conditions at the same time point of 25HC treatment (**d** and **k-m**). Statistical significance was determined by Student's t-test with a Welch's correction (**a-d** and **j-m**) or an Ordinary one-way ANOVA (**i**). Exact *p*-values are reported in the Methods.

130 mapped to intron 52, which truncates ACC1 at its carboxyltransferase domain (**Extended data**
131 **Fig. 1h**, **i**). Using CRISPR to generate a series of ACC1 truncations, we found that an exon 52
132 truncation behaves similarly to an exon 11 truncation lacking both catalytic domains, and is thus
133 referred to as *ACC1* KO (**Extended data Fig. 1j-l**). Surprisingly, ACC1 truncated at exon 3 was
134 lethal to cells, suggesting that ACC1 early exons have functionality beyond malonyl-CoA
135 synthesis, perhaps through a scaffolding function (**Extended data Fig. 1m**)[41]. This finding
136 highlights the strength of random insertion mutagenesis: since CRISPR libraries have sgRNAs
137 targeting early exons, they would fail to identify ACC1 as a hit due to cell lethality.
138 The lysosomal cholesterol transporters NPC1 and NPC2 are mutated in Niemann-Pick
139 disease type C (NPC disease), an incurable fatal syndrome. We and others have shown that
140 NPC1 inhibition or knockout causes reduced PM cholesterol levels (**Extended data Fig. 1n-**
141 **p**)[42]. Since the cell biological changes that drive NPC disease symptoms remain an area of
142 active research, treatments that restore cells to homeostasis could be investigated as potential
143 therapies. Remarkably, *ACC1* KO cells treated with U18666A had PM cholesterol levels
144 indistinguishable from WT untreated cells (**Fig. 1i**). To more closely mirror a chronic disease
145 state, we treated *NPC1* KO cells with the ACC1 inhibitor Firsocostat, a drug tested in human
146 clinical trials for the treatment of metabolic dysfunction-associated steatotic liver disease
147 (MASLD). Remarkably, Firsocostat elevated PM cholesterol in both *NPC1* KO HAP1 cells and
148 mouse embryonic fibroblasts; the amount of Firsocostat could be reduced so that PM
149 cholesterol abundance more closely matches control levels. This demonstrates that ACC1
150 inhibition does not raise PM cholesterol levels through a mechanism involving NPC1 (**Fig. 1j**
151 and **Extended data Fig. 1p**). We thus suggest that ACC1 inhibition could be a testable
152 treatment for NPC disease.
153 Cells protect themselves from pathogen invasion by transiently synthesizing 25HC,
154 which drives a ~10-fold reduction in PM cholesterol (**Fig. 1b**, **d**). Under non-infection conditions,
155 elevated 25HC promotes inflammation linked to elevated stroke risk, osteoarthritis,
156 atherosclerosis, and fibrosis[43–46]. Therefore, understanding how 25HC drives PM cholesterol
157 changes, and reducing these changes for healthy individuals, could have broad clinical impacts.
158 Treatment of *ACC1* KO cells with 25HC revealed a significant defect in cholesterol depletion
159 compared to WT cells, with >60% of cholesterol remaining at the PM after 6 hours (**Fig. 1k**).
160 The ACC1 inhibitor Firsocostat also prevented PM cholesterol depletion induced by 25HC in
161 HAP1, 293T and 3T3 cells, demonstrating that this response is conserved across cell types
162 from different lineages (**Fig.1l**, **m**)[47]. Given the broad importance of 25HC in human disease, we
163 set out to understand how ACC1 loss can block 25HC-mediated cholesterol trafficking.
164
165 **ACC1 functions independently of ACAT1/2 to maintain plasma membrane cholesterol**
166 **levels.**
167 Using both microscopy and flow cytometry, ACC1 loss caused a striking increase in PM
168 cholesterol in untreated cells (**Fig. 2a**, **b** and **Extended data Fig. 1k**, **l**). This effect was
169 observed in multiple cell types and with structurally distinct ACC1 inhibitors, including the
170 dimerization inhibitor Firsocostat and the carboxyltransferase domain active site inhibitor CP-
171 640186 (**Fig. 2c**, **d**)[48,49]. ACC1 loss also increased cell death caused by the cholesterol-
172 dependent cytolysin PFO* (**Fig. 2e**). PFO* binds to accessible cholesterol and above 4°C it
173 oligomerizes to generate pores in the PM[10,50]. We hypothesized that ACC1 could raise PM

174 cholesterol accessibility by reducing sphingomyelin levels since sphingomyelin binds and
175 sequesters cholesterol in the PM. Using mass spectrometry, a sphingomyelin-binding probe,
176 and a sphingomyelinase assay, we showed that ACC1 loss does not change sphingomyelin
177 levels (**Extended data Fig. 2a-d**). Altogether, our data suggests that ACC1 is critical for
178 maintaining PM cholesterol in untreated cells.
179 25HC-driven PM cholesterol depletion was previously shown to require ACAT1 and
180 ACAT2; these proteins esterify cholesterol with a fatty acid, promoting its storage in lipid
181 droplets[20]. We hypothesized that ACC1 loss reduces the pool of available fatty acids that are
182 used by ACAT1/2 to make cholesterol esters (CEs) (**Fig. 2f**). If cholesterol cannot be stored, PM
183 cholesterol may rise as observed in *ACC1* KO cells. To test this, we treated cells with the
184 ACAT1/2 inhibitor SZ58-035, which blocked CE formation induced by 25HC (**Extended data**
185 **Fig. 2e**)[51]. ACAT1/2 inhibition reduced PM cholesterol depletion induced by 25HC, however the
186 magnitude of the effect was small compared to previous reports and also less than what was
187 observed for ACC1 inhibition (**Extended data Fig. 2f** and **Fig. 1k**)[20]. Therefore, we generated
188 *ACAT1/2* double knockout (DKO) cells with a dual-sgRNA CRISPR strategy (**Fig. 2g**). As
189 expected, *ACAT1/2* DKO cells showed undetectable levels of CEs (**Fig. 2h**). Similarly to SZ58-
190 035 treated cells, *ACAT1/2* DKO cells showed reduced cholesterol depletion in response to
191 25HC compared to WT cells, however, in contrast to previous reports, a significant fraction of
192 PM cholesterol was still depleted (**Fig. 2i**)[20].
193 If ACC1 and ACAT1/2 are acting in the same pathway, then knocking out ACC1 and
194 ACAT1/2 together should not have a combinatorial effect. We treated *ACAT1/2* DKO cells with
195 ACC1 inhibitor, which caused a dramatic increase in PM cholesterol in the presence of 25HC
196 (**Fig. 2j**). Additionally, ACAT1/2 inhibition further blunted the effect seen in *ACC1* KO cells
197 (**Extended data Fig. 2g**). Finally, we made a triple knockout (TKO) cell line lacking ACC1,
198 ACAT1 and ACAT2, which had an additive effect compared to knocking out either ACC1 or
199 ACAT1/2 alone (**Fig. 2k**, **l**). Moreover, the PM cholesterol levels of *ACAT1/2* DKO cells were not
200 significantly different from WT cells in agreement with previous reports[20]. Inhibition of ACC1 in
201 *ACAT1/2* DKO cells led to a dramatic increase in PM cholesterol (**Fig. 2m**). These epistasis
202 experiments cleanly demonstrate that ACC1 acts through a distinct pathway from the ACAT1/2
203 proteins.
204 25HC can deplete *total cellular cholesterol* through multiple known pathways: 1)
205 LXR/ABC transporter-driven cholesterol efflux, 2) INSIG activation leading to reduced
206 cholesterol synthesis, 3) ACAT1/2-mediated cholesterol esterification, and 4) by elevating the
207 expression of oxysterol-producing enzymes like CH25H[20,26,52]. With the exception of LXR-driven
208 cholesterol efflux, which we previously showed had minor effects (**Fig. 1d**), the remaining
209 mechanisms all require cholesterol to leave the PM in order to reveal a depletion. We observed
210 a decrease in total cellular cholesterol upon 25HC treatment in WT cells, but not in *ACC1* KO
211 cells, further suggesting that ACC1 loss traps cholesterol at the PM (**Fig. 2n**). Additionally,
212 blocking HMGCR activity with a statin had minimal effects on PM cholesterol after 6 hours,
213 suggesting that the reduced PM cholesterol we observed is not due to reduced synthesis
214 (**Extended data Fig. 2h**).

Fig. 2: ACC1 functions independently of ACAT1/2 to maintain plasma membrane cholesterol levels.

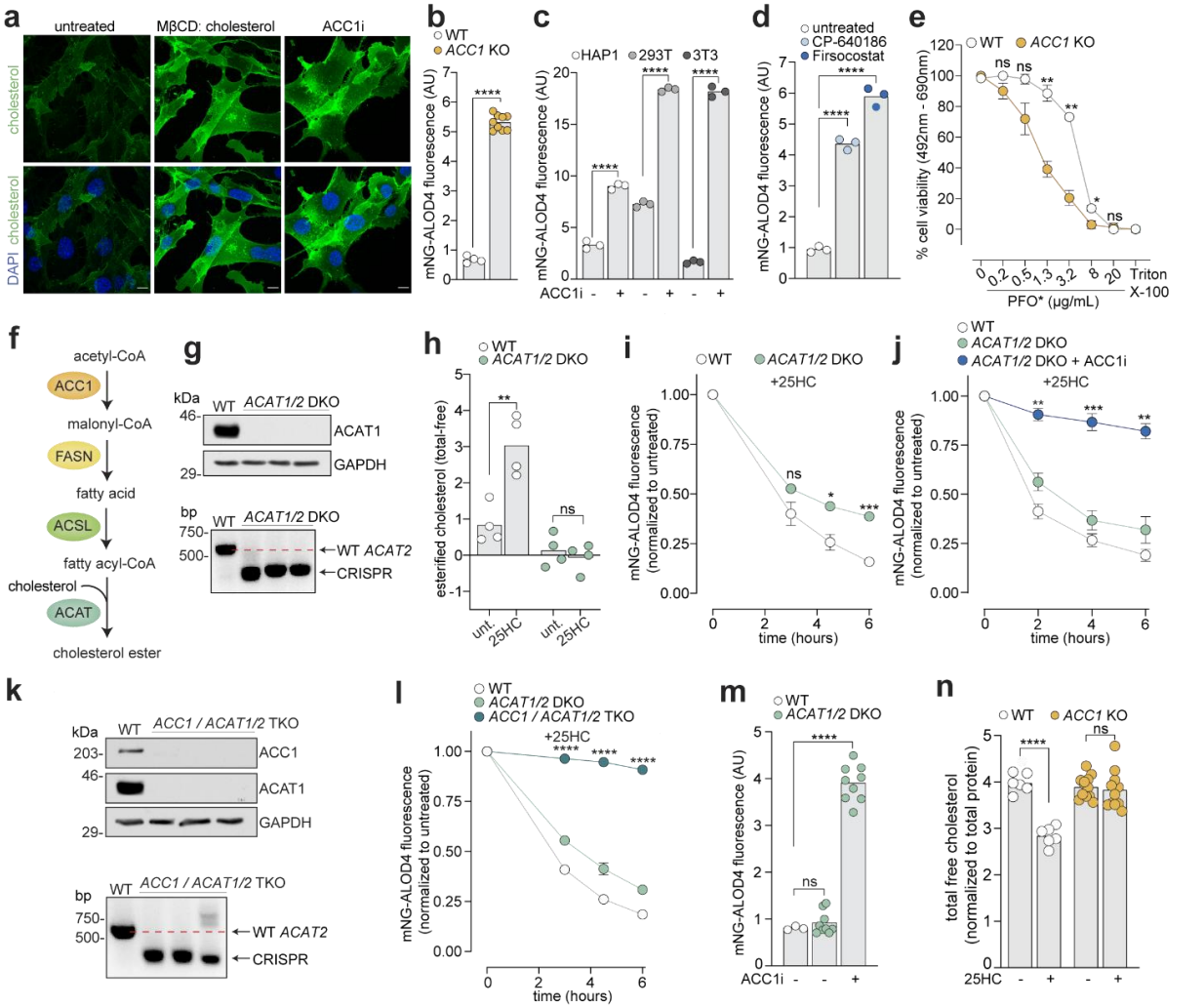

a, Fluorescence microscopy image showing wild-type (WT) 3T3 cells left untreated or treated with 0.3 mM MβCD:cholesterol or ACC1i (30 μM Firsocostat) and stained with mNG-ALOD4 and DAPI. Scale bar is 10 microns. **b-d**, Cell lines were left untreated (**b**) or treated with 30 μM Firsocostat (**c**) or 20 μM CP-640186 for 16 hrs (**d**) and then stained with mNG-ALOD4 and analyzed by flow cytometry. **e**, Cells were treated with 4 μM 25HC for 4 hrs and then media was replaced with PFO* for 30 minutes at 37°C before cell viability was measured with an XTT assay. **f**, Schematic of cholesterol ester synthesis. ACAT1 and ACAT2 (ACAT) enzymes transfer a fatty acid from acyl-CoA to cholesterol, forming cholesterol esters. **g**, Western blot (ACAT1) and PCR (*ACAT2*) analysis of *ACAT1/2* DKO clones. **h**, WT and *ACAT1/2* DKO cell lines were treated with 4 μM 25HC for 6 hrs and the esterified cholesterol was quantified using the Amplex Red assay. **i**,**j**, Cells were left untreated (**i**) or treated for 16 hrs with ACC1i (30 μM Firsocostat) (**j**); cells were then treated with 4 μM 25HC for the times indicated and then the amount of mNG-ALOD4 bound to the PM was measured by flow cytometry. **k**, Western blot (ACAT1 and ACC1) or PCR (*ACAT2*) analysis of *ACC1/ACAT1/2* TKO clones**. l**, Cells were treated with 4 μM 25HC for the indicated times and then mNG-ALOD4 staining was measured by flow cytometry. **m**, mNG-ALOD4 flow cytometry analysis of PM cholesterol in WT and *ACAT1/2* DKO HAP1 cells left untreated or treated with ACC1i (30 μM Firsocostat) for 16 hrs. **n,** Quantification of total cellular free (unesterified) cholesterol in WT HAP1 cells or *ACC1* KO HAP1 cells treated with or without 4 μM 25HC for 8 hrs. Cells (**b**, **d**, and **m**) were grown in lipoprotein depleted serum media for 16 hours prior to treatments. For each condition (**i**,**j** and **l**), data is normalized to cells not treated with 25HC, and each data point represents the average of three biological replicates, with error bars denoting the standard deviation. Statistical significance was determined by a Student's t-test with a Welch's correction (**b**,**c**,**h-j**, **l** and **n**) or an Ordinary one-way ANOVA (**d,** and **m**). Exact *p*-values are found in the Methods.

Lipid droplet catabolism increases plasma membrane cholesterol.

Interestingly, ACC1 inhibition caused rapid changes in PM cholesterol levels. Treatment with Firsocostat resulted in observable effects in 2 hours in HAP1 cells and in 15 minutes in 3T3 cells (**Fig. 3a** and **Extended data Fig. 3a**). These changes are not consistent with the induction of a transcriptional program like SREBP2 signaling, which should show a lag as new genes are synthesized. Consistent with SREBP2 independent effects, treatment of cells with the HMGCR inhibitor Lovastatin did not reverse the effect of ACC1 loss on PM cholesterol (**Extended data Fig. 3b**, **c**)[53]. How does ACC1 loss cause elevated PM cholesterol?

We used immunofluorescence imaging to observe ACC1 in cells and found the formation of ring-like puncta. Co-staining with Bodipy 493:503 revealed that ACC1 localizes on the surface of lipid droplets (LD), which was further confirmed through density gradient centrifugation (**Fig. 3b** and **Extended data Fig. 3d**). ACC1 was previously identified in a LD-proximity labeling study, though its localization at LDs was not further explored[54,55]. We found that ACC1 loss-of-function caused a striking reduction in LD numbers, suggesting that ACC1 activity controls LD abundance[56]. Overnight treatment with the ACC1 inhibitor Firsocostat decreased the median number of LDs per cell from ~six to zero and *ACC1* KO cells lacked LDs (**Fig. 3c** and **Extended data Fig. 3e**).

LDs have a hydrophobic core made of triacylglycerol (TAG) and CE; the TAG/CE ratio is cell-type dependent with TAG making up the major component in most cell types[57–59]. The abundance of LDs in a cell is determined by a balance of synthesis and degradation. We observed that blocking LD synthesis by inhibiting the TAG-synthesizing enzymes DGAT1 and DGAT2 did not eliminate LDs after 24 hours (**Fig. 3d** and **Extended data Fig. 3f**). These drug treatments were robust since they blocked new LD formation induced by exogenous oleic acid (OA) addition. This suggests that blocking synthesis does not cause rapid changes in LD numbers. In contrast, inhibition of ACC1 caused a 50% depletion in LD numbers after ~6 hours in lipoprotein-depleted serum (LDS) media (**Fig. 3e**). The same assay performed in lipoprotein-replete 5% fetal bovine serum (FBS) showed slower kinetics, with 50% depletion after ~10 hours (**Fig. 3f**). We therefore propose that ACC1 inhibition triggers LD catabolism, which is further explored in Figure 4. We hypothesize that catabolism occurs more robustly in LDS media because catabolic enzymes are more active under conditions of nutrient deprivation. For example, the rate limiting enzyme in TAG breakdown, adipose triacylglycerol lipase (ATGL), is activated by AMPK when cellular energy stores are low[60]. LD numbers showed a striking inverse correlation with PM cholesterol levels in both LDS and FBS, leading us to speculate that LD loss could cause an increase in PM cholesterol (**Fig. 3e**, **f**).

If LDs are indeed required for PM cholesterol trafficking, then we should be able to demonstrate this through orthogonal mechanisms. Knockout of FASN, the enzyme acting downstream of ACC1 to generate fatty acids, showed reduced LD numbers and a ~2.5-fold increase in PM accessible cholesterol (**Extended data Fig. 3g-i**). *FASN* KO also caused a defect in cholesterol trafficking in response to 25HC (**Extended data Fig. 3j**). The effects of *FASN* KO were overall smaller than those measured for *ACC1* KO, which we speculate was due to poor cell health; for example, these cells required growth in 20% FBS-containing media in order for survival. High serum likely provides significant exogenous fatty acids, which may mask the full impact of FASN loss. The FASN inhibitor C75 caused no change to PM cholesterol levels, and also did not induce LD catabolism after 48 hours (**Extended data Fig. 3k**). This

suggests that in contrast to ACC1 inhibition, FASN inhibition does not trigger LD catabolism; interestingly, FASN did not colocalize with LDs (**Extended data Fig. 3l**).

Fig. 3: Lipid droplet catabolism increases plasma membrane cholesterol.

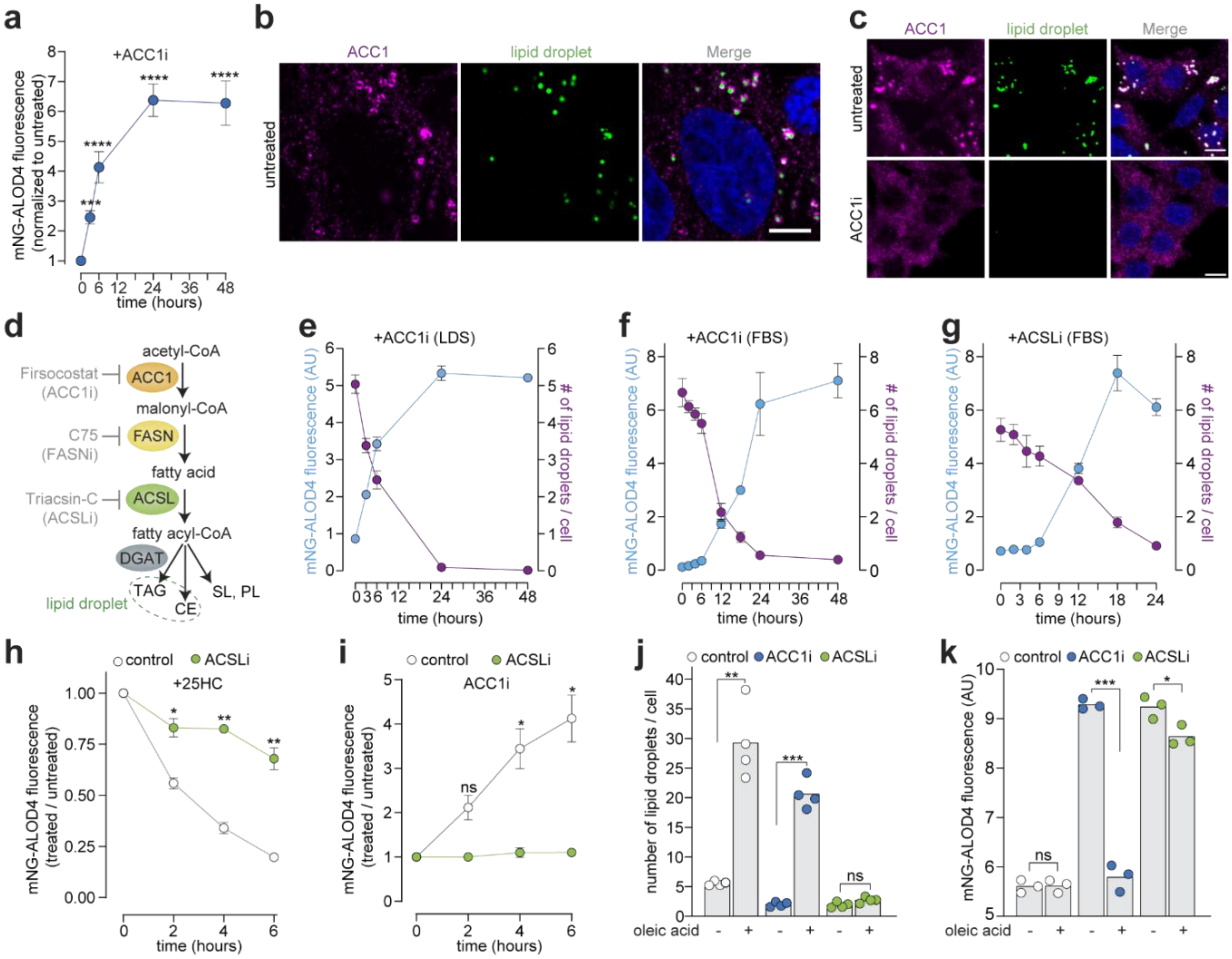

a, Plasma membrane (PM) cholesterol was measured by mNG-ALOD4 staining followed by flow cytometry in WT HAP1 cells treated with ACC1i (30 μM Firsocostat) for the indicated times. **b**,**c**, Microscopy images of HAP1 cells left untreated or treated with ACC1i (30 μM Firsocostat), and then stained with ACC1 monoclonal antibody (**b**) or 647-conjugated ACC1 polyclonal antibody (**c**), Bodipy 493/503 to measure lipid droplets (LDs) and DAPI (blue). Scale bar is 5 microns. **d**, Schematic showing that enzymes involved in the synthesis of fatty acyl-CoAs, which are then converted into triacylglycerol (TAG), cholesterol esters (CE), sphingolipids (SL) and phospholipids (PL). TAG and CE are the main components of the LD core (green oval). Inhibitors targeting enzymes in this process are shown in gray. **e**-**g** mNG-ALOD4 flow cytometry analysis of PM cholesterol (blue curves) and the corresponding fluorescence microscopy quantification of the number of LDs per cell (purple curves) in HAP1 cells grown in 5% LDS (**e**) or 5% FBS (**f**,**g**) and then treated with ACC1i (30 μM Firsocostat) (**e**,**f**) or ACSLi (5 μM Triacsin-C) (**g**). LDs were quantified by taking the mean number of LDs per cell in four fields of view with ~75 cells per field. **h**,**i**, mNG-ALOD4 flow cytometry analysis of PM cholesterol in WT HAP1 cells treated with or without ACSLi (5 μM Triacsin-C) for 16 hrs in 5% LDS, followed by treatment with 4 μM 25HC (**h**) or 30 μM ACC1i (**i**) for the indicated times. **j**,**k**, LD quantification (**j**) and mNG-ALOD4 flow cytometry analysis of PM cholesterol (**k**) of WT HAP1 cells treated with or without 30 μM ACC1i or 5 μM ACSLi for 16 hrs, followed by 200 μM oleic acid treatment for 6 hrs in 5% FBS. Each flow cytometry data point (**e**-**i**) represents the mean of three biological replicates, with error bars indicating the standard deviation. Values were normalized to the untreated control at the corresponding time point. Statistical significance was determined by Ordinary one-way ANOVA (**a**) or Student's t-test with a Welch's correction (**h**-**k**). Exact *p*-values are found in the Methods.

264 The most common method to acutely reduce LD numbers is treatment with the acyl-CoA
265 synthetase long-chain (ACSL1,3-6 are henceforward collectively called ACSL) inhibitor Triacsin-
266 C, which both prevents LD synthesis and stimulates LD catabolism by starving the cell of fatty
267 acyl-CoA (**Fig. 3d**)[61,62]. Remarkably, ACSL inhibition led to an ~8-fold increase in PM cholesterol
268 levels that inversely correlated with LD levels (**Fig. 3g**). ACSL inhibition showed a maximal
269 effect on PM cholesterol after ~18 hours; at 24 hours, PM cholesterol started to decrease and at
270 48 hours cell death occurred. Similarly to ACC1 loss, ACSL loss also robustly blocked PM
271 cholesterol depletion induced by 25HC (**Fig. 3h**). This provides additional evidence that LDs
272 mediate cholesterol trafficking out of the PM in response to 25HC. To test whether ACC1 and
273 ACSLs were acting in the same pathway, we treated cells overnight with Triacsin-C to eliminate
274 LDs, and then performed a Firsocostat treatment time course. In cells lacking LDs, ACC1
275 inhibition had no added effect on PM cholesterol levels (**Fig. 3i**). This result suggests that the
276 differences we observe upon ACC1 inhibition arise from changes in LD numbers; if LDs are
277 absent to begin with, ACC1 does not cause further changes.
278 If trafficking of cholesterol out of the PM requires LDs, then the addition of exogenous
279 OA should reverse the ACC1 phenotype. Treatment with 6 hours of OA elevated the number of
280 LDs in both control cells and ACC1 inhibited cells (**Fig. 3j**). Importantly, ACSL inhibition blocked
281 LD formation induced by OA treatment, since ACSL enzymes are required to convert fatty acids
282 into fatty acyl-CoAs, the precursors for both TAG and CE. OA reversed the high PM cholesterol
283 levels of ACC1 inhibited cells but not ACSL inhibited cells (**Fig. 3k**). The finding that OA addition
284 to cells can reverse the effects of ACC1, but not ACSL, provides strong evidence that LDs are
285 the crucial mediator of PM cholesterol trafficking.
286
287 **ACC1 inhibition triggers lipid droplet catabolism through ATGL.**
288 Since both ACC1 and ACSL loss raised PM cholesterol levels, we hypothesized that cholesterol
289 homeostasis is controlled by a common product of these enzymes, which could include fatty
290 acyl-CoAs or LDs made of TAG (**Fig. 4a**). ATGL is the rate limiting enzyme in LD catabolism,
291 hydrolyzing TAG to generate diacylglycerol (DAG) and a fatty acid[63]. To test if TAG breakdown is
292 required for the PM cholesterol changes seen upon ACC1 inhibition, we generated CRISPR
293 knockouts of ATGL (**Fig. 4b**). *ATGL* KO cells showed similar numbers of LDs compared to WT
294 cells, although they were significantly larger in size (**Fig. 4c**, **d**). When ACC1 was inhibited, WT
295 cells showed a ~50% depletion in LD numbers after six hours. In contrast, *ATGL* KO cells
296 showed no change in LD numbers with six hours of ACC1 inhibition (**Fig. 4e**-**g**). This suggests
297 that ACC1 inhibition triggers ATGL-dependent LD catabolism.
298 ACC1 inhibition leads to a rapid increase in PM cholesterol in WT cells. Importantly, the
299 effects of ACC1 inhibition were largely blocked in *ATGL* KO cells, which we propose is due to
300 the stable LD population (**Fig. 4h**). The newly characterized human-specific inhibitor of ATGL,
301 NG-497, also blocked PM cholesterol changes induced by ACC1 loss of function (**Fig. 4i**)[64].
302 ATGL inhibition also reversed the defect in 25HC-induced cholesterol transport observed in
303 ACC1 inhibited cells (**Extended data Fig. 4a**). These data demonstrate that ACC1 inhibition
304 causes PM cholesterol changes by depleting cells of LDs, and not through another mechanism.
305 When TAG is hydrolyzed by ATGL, a fatty acid is liberated, which can then be converted into a
306 fatty acyl-CoA by ACSL enzymes (**Fig. 4a**). The ability of *ATGL* KO to reverse the ACC1

phenotype argues against fatty acyl-CoA's playing a role in PM cholesterol homeostasis since ATGL loss further reduces fatty acyl-CoA levels.

We hypothesized that PM cholesterol rises upon LD catabolism because CEs are hydrolyzed, and subsequently the newly liberated (unesterified) cholesterol traffics to the PM. To test this, we imaged LDs in *ACAT1/2* DKO cells, which had slightly reduced LD numbers compared to WT cells, though LD size was unaltered (**Extended data Fig. 4b-d**). ACC1 inhibition induced LD loss in *ACAT1/2* DKO cells similarly to WT cells (**Extended data Fig. 4e**). Finally, Firsocostat treatment raised PM cholesterol levels in *ACAT1/2* DKO cells (lacking CE), although with slightly reduced kinetics compared to WT cells (**Extended data Fig. 4f**). These results suggest that CE hydrolysis partially contributes to the *initial* increases in PM cholesterol seen upon ACC1 inhibition. Our data showing that *ACC1* KO leads to a sustained increase (over weeks of passage) in PM cholesterol suggests that LDs loss has long lasting effects on cellular cholesterol (**Fig. 2b**, **Extended data Fig. 1k**). Cells lacking ACC1 are not able to return to the WT homeostatic set point of PM cholesterol.

Fig. 4: ACC1 inhibition triggers lipid droplet catabolism through ATGL.

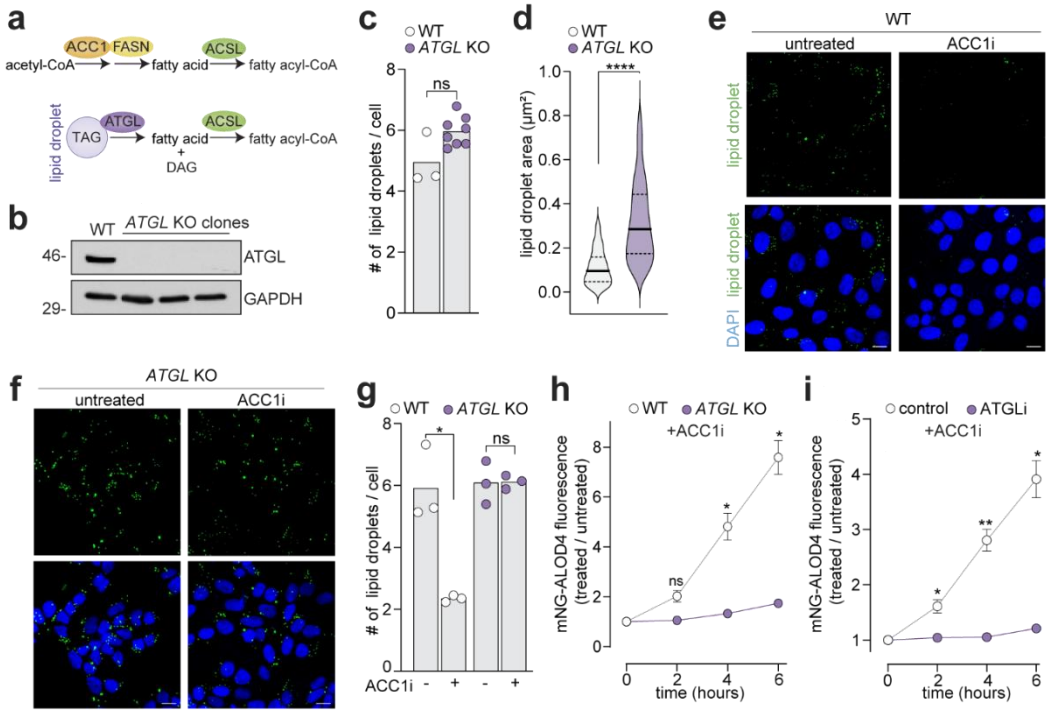

a, Schematic illustrating the formation of fatty acyl-CoAs from de novo synthesis of fatty acids (top) or from the breakdown of triacylglycerol (TAG) into diacylglycerol and a fatty acid by ATGL (bottom). ATGL localizes at the lipid droplet (LD) surface. **b**, Western blot analysis of *ATGL* KO HAP1 cells compared to a wild-type (WT) control. **c**,**d**, Quantification of LD numbers per cell (**c**) or LD area (**d**) in WT and *ATGL* KO cells. **e-g** Microscopy images (**e**,**f**) and quantification (**g**) of LDs in WT (**e**) and *ATGL* KO (**f**) HAP1 cells treated with or without ACC1i (30 μM Firsocostat) for 6 hrs. Cells were stained with Bodipy 493/503 and DAPI (blue). Scale bar is 5 microns. Each data point is the total number of LDs per cell in a single field of view, with ~75 cells per field (**c** and **g**). **h**, **i**, mNG-ALOD4 flow cytometry analysis of PM cholesterol in WT and *ATGL* KO cells (**h**) or WT cells treated with or without ATGLi (50 μM NG-497) (**i**), followed by treatment with ACC1i (30 μM Firsocostat) for the indicated times. All experiments were carried out in cells pre-cultured for 16 hours in lipoprotein depleted serum. Data points represent the average of three biological replicates, with error bars indicating the standard deviation. All values were normalized to the untreated control (**h**,**i**). Statistical significance was determined by a Student's t-test with a Welch's correction (**c**,**d** and **g-i**). Exact *p*-values are found in the Methods.

322
323 **Increasing lipid droplet abundance reduces plasma membrane cholesterol.**
324 What is the consequence of increasing LD numbers? We found that the ATGL inhibitor NG-497
325 increased LD numbers in cells (**Fig. 5a**, **b** and **Extended data Fig. 5a**). This contrasts the *ATGL*
326 KO cells which showed enlarged but not more numerous LDs; it is not uncommon for knockout
327 cell lines to show different effects compared to drug treatments since cells will adapt to the
328 chronic loss of a gene. Interestingly, ATGL inhibition caused a ~7-fold decrease in PM
329 cholesterol levels (**Fig. 5c** and **Extended data Fig. 5b**). This data suggests that elevating LD
330 numbers reduces PM cholesterol. Combined treatments of the ATGL inhibitor with an ACC1 or
331 ACSL inhibitor showed intermediate effects on LD numbers at 24-hour time points. In all cases,
332 PM cholesterol showed a clear inverse relationship with LD numbers. We next sought to
333 increase LD numbers through an orthogonal mechanism.
334 AMPK plays central roles in cellular energy metabolism by controlling the balance
335 between anabolic and catabolic processes. When cellular energy stores are low, AMPK inhibits
336 anabolic proteins such as ACC1, HMGCR and RAPTOR, a member of the mTORC1 complex.
337 Conversely, AMPK activates catabolic enzymes like ATGL, CPT1 and ULK1, which, together
338 with mTORC1 inhibition, promotes autophagic flux (**Fig. 5d**)[65,66]. We therefore asked whether
339 AMPK inhibition would change LD numbers by activating ACC1 and simultaneously inhibiting
340 ATGL. Treatment of cells with the AMPK inhibitor Dorsomorphin (also named Compound C)
341 reduced the levels of phosphorylated inactive ACC1, which is expected to increase the active
342 ACC1 pool (**Fig. 5e**)[67]. Consistent with ACC1 activation leading to elevated fatty acid synthesis,
343 AMPK inhibition led to a ~2-fold increase in the number of LDs per cell (**Fig. 5f**, **g**). This effect
344 appeared to be driven by ACC1 activity rather than ATGL inactivation, because treatment with
345 the ACC1 inhibitor Firsocostat reversed the changes in LD numbers.
346 Elevating LD numbers by inhibiting AMPK caused a ~5-fold decrease in PM accessible
347 cholesterol levels (**Fig. 5h**). This provides further evidence that elevating LD abundance can
348 reduce PM cholesterol, possibly by enhancing its transport out of the PM. Alternatively, ACC1
349 activation could reduce PM cholesterol by increasing the availability of fatty acids for cholesterol
350 esterification thereby promoting the conversion of free cholesterol into CEs. We show this is
351 unlikely because AMPK inhibition elevated LD numbers and reduced PM cholesterol in *ACAT1/2*
352 DKO cells similarly to WT cells (**Fig. 5i**, **j**). Surprisingly, OA treatment, which causes the rapid
353 formation of large LDs, did not reduce PM cholesterol below WT levels, despite reversing the
354 effects of ACC1 inhibition (**Fig. 3j, k**). Analysis of OA-induced LDs by microscopy showed that
355 they had reduced ACC1 localization at their surface, compared to untreated cells or cells treated
356 with ATGL or AMPK inhibitors (**Extended data Fig. 5c**). This suggests that LDs formed from OA
357 addition may partially lack proteins that are important for LD localization, function, or LD-
358 organelle contact sites. In conclusion, two structurally distinct inhibitors that raise LD numbers
359 both cause a decrease in PM cholesterol levels. These findings provide additional evidence that
360 LDs are important for PM cholesterol homeostasis.

Fig. 5: Increasing lipid droplet abundance reduces plasma membrane cholesterol.

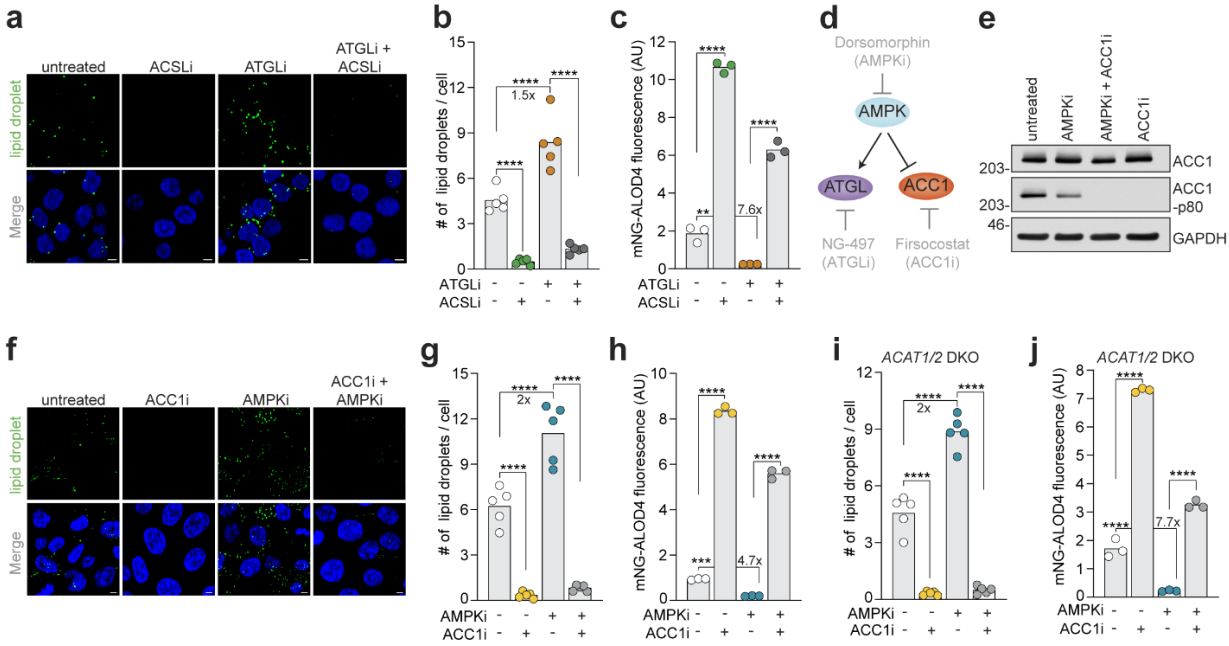

a-c, Wild-type (WT) HAP1 cells were left untreated or treated with ACSLi (5 μM Triacsin-C), ATGLi (50 μM NG-497) or both for 16 hrs and then analyzed by microscopy to quantify lipid droplet (LD) numbers per cell (**a**, **b**) or by mNG-ALOD4 flow cytometry analysis to determine plasma membrane (PM) cholesterol levels (**c**). **d**, Schematic demonstrating that AMPK inactivates ACC1 and activates ATGL. Inhibitors for each enzyme are shown in gray. **e**, Western blot analysis of ACC1 phosphorylation in WT HAP1 cells left untreated or treated with AMPKi (2.5 μM Dorsomorphin), ACC1i (30 μM Firsocostat) or both. **f-h** WT HAP1 cells were left untreated or treated with 30 μM ACC1i, 2.5 μM AMPKi or both and then analyzed by microscopy to quantify LD numbers per cell (**f**, **g**) or by mNG-ALOD4 flow cytometry analysis to determine PM cholesterol levels (**h**). **i**,**j**, LD quantification (**i**) and flow cytometry analysis of PM cholesterol using mNG-ALOD4 staining (**j**) in *ACAT1/2* DKO cells left untreated or treated with 2.5 μM AMPKi, 30 μM ACC1i or both. All cells were grown in lipoprotein depleted serum media for 16 hours prior to drug treatments. Lipid droplets are visualized with Bodipy 493:503 and nuclei are visualized with DAPI. Scale bars are 5 microns. Statistical significance was determined by an Ordinary one-way ANOVA (**b-c** and **g-j**). Each data point is the total number of LD per cell in a single field of view (**b**,**g** and **i**). Exact *p*-values are found in the Methods.

ACC1 loss traps accessible cholesterol at the plasma membrane and triggers de novo cholesterol synthesis in a mouse model.

To strengthen our findings, we extended our studies with an animal model. In hepatocytes, ACC2 contributes to the synthesis of ~10% of cellular fatty acids[68]. Therefore, we induced recombination-mediated removal of both ACC1 and ACC2 using Albumin-CRE *Acc1/Acc2* flox/flox mice (with flox sites around exon 21/22 and 26/27 for ACC1 and ACC2, respectively) to generate a double liver knockout of *Acc1/Acc2* [68]. Hepatocytes isolated from *Acc1/Acc2* dLKO mice showed undetectable levels of ACC1 and ACC2 proteins, and fatty acid synthesis was markedly reduced (**Fig. 6a**, **b**). These hepatocytes also showed a reduction in TAG and CE levels compared to controls (**Fig. 6c**, **d**).

Strikingly, dLKO primary hepatocytes showed a 10-fold increase in PM cholesterol (**Fig. 6e**, **f**). These data highlight that ACC1 loss leads to a sustained increase in PM cholesterol that cannot be restored to WT levels in vivo. Liver cells are specialized to export total cellular cholesterol, both as VLDL and as bile acids[69,70]. The inability of cells lacking ACC1 to restore

376 their PM cholesterol levels suggests that ACC1 is a critical component of cholesterol
377 homeostasis machinery.
378 Trapping cholesterol at the PM is expected to reduce ER-localized cholesterol and
379 trigger de novo cholesterol biosynthesis. To test the cellular response to ACC1 loss in an
380 unbiased way, we performed RNA sequencing on cells treated with inhibitors against either
381 ACC1 (Firsocostat), ACSL (Triacsin-C), HMGCR (Lovastatin) or FASN (C75). Throughout this
382 work, we showed that ACC1 and ACSL inhibition reduced LD numbers and increased PM
383 cholesterol (**Fig. 3**); in contrast, HMGCR inhibition reduced PM cholesterol (**Extended data Fig.**
384 **3b**, **c**), and FASN inhibition did not change LD or PM cholesterol levels (**Extended data Fig.**
385 **3k**). FASN inhibition serves as a useful control for ACC1 inhibition, since both conditions block
386 fatty acid synthesis. Strikingly, we observed that ACC1 and ACSL inhibition potently elevated the
387 expression of cholesterol biosynthesis genes, and closely resembled HMGCR inhibition (**Fig.**
388 **6g**). To the best of our knowledge, prior to this work, there was no known mechanism to explain
389 why blocking fatty acid biosynthesis would trigger SREBP2 activation. FASN inhibition had small
390 to no effects on SREBP2 targets, consistent with its inability to trigger LD breakdown. Inspection
391 of SREBP2 target gene induction across treatments yielded unexpected findings for future
392 studies- for example, FDFT1, the first committed step in cholesterol biosynthesis was not
393 induced by HMGCR inhibition, though it was significantly induced by ACC1 inhibition.
394 Cholesterol and fatty acid biosynthetic pathways have evolved to be coregulated, which
395 is evidenced by significant work showing that SCAP, an ER-localized cholesterol sensor,
396 controls the activation of both SREBP1 and SREBP2 transcription factors[14,71,72]. This work
397 implies that when ER cholesterol levels are low, both SREBP1 and SREBP2 target genes are
398 induced. Investigating known SREBP1 targets revealed that multiple genes (FASN, FADS2,
399 SCD, ACSL3, ACACA, and SREBP1 itself) were elevated more strongly through the inhibition of
400 ACC1 or ACSL than by HMGCR (**Fig. 6h**). This was not due to the relative potency of different
401 inhibitors since HMGCR inhibition had the strongest effects for multiple cholesterol biosynthesis
402 genes (including HMGCR, MVK, SQLE and CYP51A1). Factors such as insulin and
403 polyunsaturated fatty acids are known to regulate SREBP1 independently of SREBP2; future
404 investigations are required to determine which of these are driving the discordance seen
405 between SREBP2 and SREBP1 targets in our study[73–76].
406 To determine which pathways were most significantly affected by LD loss, we performed
407 a Gene Set Enrichment Analysis (GSEA) using the top 200 most differentially regulated genes
408 from each treatment condition (ranked by FDR-corrected *p*-value). Among the pathways
409 enriched, cholesterol metabolism was number one for both ACC1- and ACSL-inhibited cells
410 (**Fig. 6i**). All four treatments showed similar effects on VEGFA-VEGFR2 signaling and mRNA
411 processing pathways. Finally, ACSL and FASN inhibition showed multiple overlapping enriched
412 pathways. Altogether, RNA sequencing provided strong evidence that ER cholesterol is depleted
413 by ACC1 and ACSL inhibitor treatments, which supports the model that LD loss reduces
414 cholesterol trafficking out of the PM.
415 Finally, we tested cholesterol synthesis rates in the *Acc1/Acc2* dLKO primary
416 hepatocytes. Consistent with our cellular findings, radiotracing of tritiated water showed dLKO
417 hepatocytes had markedly elevated rates of cholesterol synthesis compared to controls (**Fig.**
418 **6j**). This result, combined with the observed increase in PM cholesterol levels (**Fig. 6e**, **f**),
419 suggests that ACC1 loss reduces cholesterol trafficking from the PM to the ER. Despite having

420 elevated PM cholesterol and elevated cholesterol synthesis, *total* cellular cholesterol levels were
421 not significantly elevated in vivo or in cell culture (**Fig. 6k**, **Fig. 2n** and **Extended data Fig. 6a**,
422 **b**). What is the fate of the newly synthesized excess cholesterol? Analysis of fecal cholesterol
423 levels revealed that it was excreted in mice (**Fig. 6l**). These findings demonstrate that while
424 maintaining high PM accessible cholesterol, cells undergo homeostasis to maintain total cellular
425 cholesterol levels. This observation is at odds with the dogma which states that cells sense and
426 regulate the accessible pool of cholesterol specifically. In conclusion, our study finds that ACC1,
427 the master regulator of fatty acid biosynthesis, is critical for controlling LD catabolism through
428 ATGL. Most strikingly, we show that LDs are crucial for cellular cholesterol homeostasis– their
429 loss traps cholesterol at the PM and induces de novo cholesterol synthesis in the ER (**Fig. 6m**).

Fig. 6: ACC1 loss traps cholesterol at the plasma membrane and triggers de novo cholesterol synthesis in a mouse model.

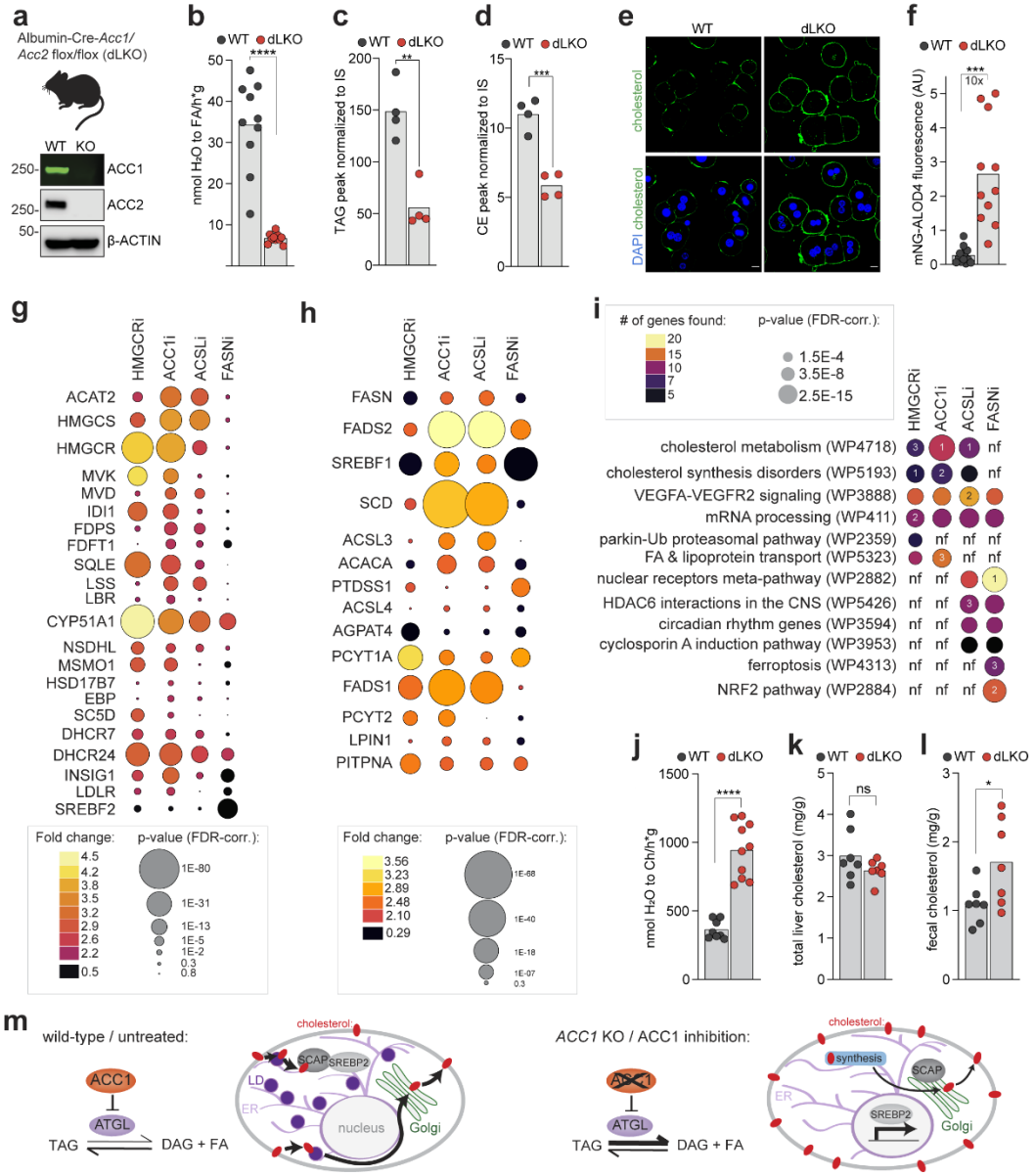

a, Western blot analysis of ACC1 and ACC2 proteins in primary hepatocytes isolated from *Acc1/Acc2* flox/flox and Albumin-Cre-*Acc1/Acc2* dLKO mice. **b-d**, Hepatic fatty acid synthesis rates (**b**), hepatic triacylglycerol (TAG) levels (**c**), and hepatic cholesterol ester (CE) levels (**d**) in *Acc1/Acc2* flox/flox and Albumin-Cre-*Acc1/Acc2* dLKO mice. **e**, Fluorescence microscopy images of primary hepatocytes stained with mNG-ALOD4 and DAPI. Scale bar is 10 microns. Quantification is shown in (**f**). **g**,**h**, Bubble plot showing differential gene expression from RNA sequencing in WT HAP1 cells. Cells were pre-cultured in lipoprotein depleted serum (LDS) media for 16 hours and then left untreated or treated for 6 hrs with HMGCRi (10 μM Lovastatin), ACC1i (30 μM Firsocostat), ACSLi (5 μM Triacsin-C) or FASNi (10 μM C75). Differential gene expression was computed by comparing each treatment to the untreated (LDS only) control. Bubble size shows the FDR-corrected *p*-value and bubble color shows the fold change (see legends) for each SREBF2 (**g**) and SREBP1 (**h**) target gene. SREBP1 target genes are ranked based on their enrichment in a ChIP-Seq dataset. **i**, Gene Set Enrichment Analysis from RNA sequencing data using the top 200 genes sorted by the FDR-corrected *p*-value. "nf" refers to not found. **j-l**, Hepatic sterol synthesis rate (**j**), hepatic cholesterol content (**k**), or fecal cholesterol measurement (**l**) in chow-fed *Acc1/Acc2* flox/flox and Albumin-Cre-*Acc1/Acc2* dLKO mice. **m,** Schematic showing a proposed model: ACC1 inhibits ATGL, blocking the breakdown of TAG to diacylglycerol (DAG) and fatty acids (FA). When ACC1 is inhibited (right), ATGL is activated, leading to TAG hydrolysis. Cell diagrams show that lipid droplets (LD) control cholesterol trafficking from the PM to the ER. When LDs are depleted (right), cholesterol becomes trapped at the PM, and SREBP2 drives the expression of cholesterol biosynthesis genes. Statistical significance was determined by a Student's t-test with a Welch's correction (**b-d, f** and **j-l**). Exact *p*-values are found in the Methods.

Discussion

In this study we set out to find new regulators of PM cholesterol levels. We were surprised to discover that ACC1, a protein extensively studied for its role in fatty acid synthesis, also regulates cellular cholesterol homeostasis. ACC1 knockout raises PM cholesterol levels 5- to 10-fold, restores PM cholesterol changes observed in NPC1-deficient cells, and also blocks PM cholesterol depletion induced by 25HC through a mechanism that is independent of cholesterol esterification by ACAT1/2. We implicate LDs as playing a critical role in cholesterol movement out of the PM. Reducing LD numbers traps cholesterol at the PM and strongly induces de novo cholesterol biosynthesis both in vitro and in an animal model. Our screen did not identify positive regulators of LD formation because many of these proteins are redundant and their knockout is not sufficient to cause LD loss– this redundancy speaks to the importance of LDs for cell survival. Given that the majority of cells in the human body have LDs, the mechanism we have discovered could represent a broad principle of cholesterol trafficking[77,78].

PM accessible cholesterol levels are thought to be faithfully maintained by continuous transport to the ER, where sensors like SCAP, ACAT1/2, and GRAMD1B localize[10,11,79]. Our discovery that LD loss causes a sustained increase in PM accessible cholesterol is surprising, and suggests that LDs are essential for the trafficking of a large pool of PM cholesterol. Why would evolution link PM-to-ER cholesterol trafficking to LD levels? We draw inspiration from the seemingly peculiar and inelegant arrangement observed in animal cells: SCAP controls both SREBP1 (fatty acid) and SREBP2 (cholesterol) activation, and yet SCAP is solely a cholesterol sensor[71]. Why not independently couple fatty acid sensing to fatty acid synthesis and cholesterol sensing to cholesterol synthesis? We believe our work raises an intriguing hypothesis to reconcile this mystery– LD levels convey information about fatty acid storage. When fatty acid storage is low (LDs are low), cholesterol cannot effectively traffic to the ER, leading to the activation of both SREBP1 and SREBP2. Conversely, when lipid storage is high and LDs are abundant, cholesterol trafficking is intact, which blocks de novo lipid synthesis; in other words, it is disadvantageous to make new lipids when significant lipids are already stored.

This paper raises the question of how LDs control cholesterol trafficking. LDs within a single cell are heterogeneous, with unique protein binding and organelle contact sites, suggestive of distinct functions[57,59]. We propose two hypotheses for how LDs control PM cholesterol transport. First, when cholesterol molecules are trafficked out of the PM, they may move onto the LD phospholipid monolayer. The LD monolayer could either accumulate cholesterol, or this membrane may act as a bridge intermediate between the PM and another organelle such as the ER. Secondly, LDs may be required for endosome maturation[80]. In this model, a loss of LDs causes early endosomes to recycle more rapidly, which would resemble a defect in cholesterol trafficking out of the PM and cause PM cholesterol to rise if anterograde trafficking of cholesterol is intact. Future studies will distinguish between these models.

While our study provides valuable insights into the role of ACC1 inhibition in promoting LD catabolism by ATGL, further investigation is needed to fully elucidate the molecular mechanism underlying this process. ATGL is known to be regulated by AMPK, however, we observed ACC1 inhibition induced LD breakdown even in the presence of AMPK inhibition, suggesting that ATGL activation was AMPK independent. We propose that ACC1 could directly inhibit ATGL through an unknown mechanism– when ACC1 is inactivated or lost, ATGL

becomes active and LDs are broken down. Future studies will be needed to determine how ACC1 triggers LD catabolism through ATGL.

Our study has implications for the myriad of disease pathologies being linked to the enzyme CH25H and its product 25HC. Recent publications show that CH25H has roles beyond pathogen evasion; its expression can promote diabetes, microglial activation, adipose tissue inflammation and fibrosis[43–45,81]. We show that ACC1 is required for 25HC-induced cholesterol trafficking out of the PM, and suggest that ACC1 inhibitors could reverse some of the disease pathologies linked to elevated 25HC levels. Additionally, LDs play clear roles in metabolic syndromes, and they have also been linked to changes in neuronal function and neurodegeneration[82,83]. ACC1 inhibition could alleviate LD-driven disease symptoms by triggering their catabolism. For example, we find that Firsocostat more robustly, and with less toxic effects, eliminates LDs compared to Triacsin-C, a previous gold standard in the field. In conclusion, we find a novel function of ACC1 in ATGL activation and LD homeostasis, and also demonstrate that LDs control PM cholesterol transport.

Acknowledgements

We thank Dr. Yvonne Lange, Dr. Theodore Steck, Dr. Pehr Harbury and Dr. Giovanni Luchetti for helpful discussions.

Funding: MK was supported by GM118082, the Ara Parseghian Medical Research Foundation, the Howard Hughes Medical Institute Hanna H. Gray Fellows Program and 5DP5OD03615502. RR was supported by GM118082 and the Ara Parseghian Medical Research Foundation; CBK was also supported by GM118082. JAO was supported by R01DK128099. KMW, EOS and SL were supported by 5DP5OD03615502. SC was supported by a Fellowship from the Arc Institute. ET was supported by the Stanford Community College Outreach Program (CCOP), with funding provided by the Biochemistry Department at Stanford University and an anonymous donor gift to CCOP. CK was supported by P01HL160487 and P30DK127984. DT was supported by the Intramural Research Program of the National Cancer Institute at the National Institutes of Health. AL was supported by the Center for Cancer Research, National Cancer Institute, National Institutes of Health Intramural Research Program project number ZIA BC 011901.

Competing Interests: JAO is a member of the scientific advisory board for Vicinitas Therapeutics.

Materials and Methods

Cell culture

HAP1 cells were grown in HyClone Isocove's Modified Dulbecco's Medium (IMDM) (SH30228FS, Fisher/Cytiva), supplemented with 5% Fetal Bovine Serum (FBS) (F0926, Millipore Sigma), 2 mM L-glutamine (MT25005CI, Fisher/corning), Penicillin (50 U/mL) and Streptomycin (50 µg/mL) (15140122, Fisher/Gibco).

517 3T3 and 293T cells were cultured in HyClone™ Dulbecco's Modified Eagles Medium
518 (SH30081FS, Fisher/Cytiva), enriched with 10% FBS (F0926, Millipore Sigma), 2 mM L-
519 glutamine (MT25005CI, Fisher/Corning), Penicillin (50 U/mL) and Streptomycin (50 µg/mL)
520 (15140122, Fisher/Gibco), 1 mM sodium pyruvate (11360070, Fisher/Gibco), 1× MEM Non-
521 Essential Amino Acids Solution (11140050, Fisher/Gibco).
522 Lipoprotein Depleted Serum (LDS) was prepared by supplementing media with 5% LDS
523 instead of 10% FBS. To prepare LDS, FBS was incubated with Cab-o-sil (1 gram per 50 mL
524 FBS) overnight at 4°C with constant shaking. After 24 hours, the suspension was centrifuged at
525 10,000 rpm to pellet silica complexes. The supernatant was carefully decanted without
526 disturbing the pellet, followed by addition of fresh Cab-o-sil at the original 1 g/50 mL ratio. After a
527 second overnight incubation at 4°C with shaking, the suspension was centrifuged again and
528 then the supernatant was filtered through 0.2 µm filter, aliquoted and snap-frozen in liquid
529 nitrogen for future use.

530 **Drug treatments**
531 Small molecules used in this study include: 25-hydroxycholesterol (25HC) (11097, Cayman
532 Chemical), the LXR inhibitor GSK2033 (1 µM) (25443, Cayman Chemical), the NPC1 inhibitor
533 U18666A (1 µM) (10009085, Cayman Chemical) the ACC1 inhibitor Firsocostat (also named
534 GS-0976 and ND-630) (30 µM) (HY-16901, MedChemExpress), the ACC1 inhibitor CP-640186
535 (20 µM) (HY15259, MedChemExpress), the HMGCR inhibitor Lovastatin (10 µM) (10010338,
536 Cayman Chemical), the ACAT1/2 inhibitor SZ58-035 (50 µM) (S9318, Millipore Sigma), the
537 FASN inhibitor C75 (10 µM) (10005270, Cayman Chemical), the AMPK inhibitor Dorsomorphin
538 dihydrochloride (2.5 µM) (HY-13418, MedChemExpress), the long-chain fatty acyl CoA
539 synthetase (ACSL) inhibitor Triacsin-C (5 µM) (BMLEI218, Enzo), human adipose triglyceride
540 lipase (ATGL) inhibitor NG-497 (50 µM) (HY-148756, MedChemExpress), Oleic acid (200 µM)
541 (O1383,Millipore Sigma), the *DGAT1* inhibitor T863 (20 µM) (SML0539, Sigma-Aldrich) and the
542 *DGAT2* inhibitor PF-06424439 (10 µM) (PZ0233, Sigma-Aldrich). Drug treatments were carried
543 out in various media compositions indicated in the Figure legends, for 16 hours at 37°C unless
544 otherwise noted.
545 **Flow cytometry analysis of plasma membrane cholesterol**
546 The cells of interest were seeded in a 24-well cell culture plate (3 replicates for each condition)
547 aiming for ~80% confluency on the day of flow cytometry analysis. The kinetics of 25-
548 hydroxycholesterol (25HC) were measured by introducing 4 µM 25HC for various times prior to
549 flow cytometry analysis both with and without 16 hour prior incubation with the noted inhibitors.
550 To prepare cells for flow cytometry they were first rinsed with 1x Phosphate Buffered
551 Saline (PBS) (P38135, Sigma), harvested with Trypsin (0.05%) - 1x EDTA (25300120,
552 Fisher/Gibco), and quenched with 4°C 5% FBS containing IMDM (or 10% FBS containing
553 DMEM) media while gently pipetting up and down to generate a single cell suspension. Cells
554 were then transferred to a 1.5 mL eppendorf tube on ice, and then spun for 5 minutes at 4ºC
555 (HAP1 WT at 1000 x*g* and 3T3/293T at 750 x*g*). The supernatant was removed and cell pellets
556 were resuspended in ~25 µL of 2 µM mNeonGreen-ALOD4 (mNG-ALOD4) diluted in 1x Probe
557 Block Buffer (PBB- 1x PBS, 1% BSA, filter sterilized through a 0.2 µm filter). The cells were
558 incubated on ice for 12 minutes before being diluted to 150 µL in PBB, and then transferred to a
559 96-well plate. Flow cytometry was performed using the BD Accuri C6 Plus Flow Cytometer.

560 During flow cytometry single live cell populations were selected based on forward scatter (FSC)
561 versus side scatter (SSC) density plots. The fluorescence of mNG-ALOD4 was measured by
562 exciting using a 488 nm laser and detecting the emission through a 585/40 nm bandpass filter.
563 The FCS files generated from BD CSampler software were loaded to FCS Express software
564 and then exported directly to GraphPad Prism for analysis.
565
566 **Measuring sphingomyelin levels with SMase**
567 HAP1 WT cells and HAP1 *ACC1* KO cells were seeded in 5% FBS IMDM in a 24-well plate and
568 grown to ~50% confluency. Cells were then left untreated or treated for 16 hours with 30 μM
569 Firsocostat in 5% FBS IMDM. The day of the assay, cells were first washed with 1x PBS and
570 then incubated at 37 ºC with sphingomyelinase (SMase) (150 mU/mg protein,S8633, Millipore
571 Sigma) for 30 minutes to hydrolyze sphingomyelin. After incubation, the cells were washed and
572 trypsinized for flow cytometry analysis as described above.
573
574 **Measurement of free cholesterol and cholesterol esters**
575 Cells were plated in a 12-well tissue culture dish in 5% FBS IMDM media and grown to 80%
576 confluency. On the day of the assay, cells were washed with 1x PBS and lysed for 10 minutes at
577 4ºC with 150 μL of lysis buffer containing 10% glycerol, 2x Protease Inhibitor Cocktail (S8830,
578 Millipore sigma), 150 mM NaCl, 50 mM tris-HCl (pH 8), 1% NP-40 and 1 mM $MgCl_2$. The
579 Amplex Red Cholesterol Assay Kit (A12216, Invitrogen/Fischer) was used to measure the free
580 cholesterol and cholesterol esters in each sample. After lysis, lysates were diluted with an equal
581 volume of 1x reaction buffer from the kit. Total cholesterol and free cholesterol were measured
582 by preparing two working solutions (with and without cholesterol esterase) as described in the
583 assay protocol and mixing the lysates with the mastermix in a 1:1 ratio in a 96-well plate. The
584 plate was incubated at 37 ºC for 30 minutes and the fluorescence emission was measured at
585 590 nm using a microplate reader.
586
587 **Microscopy analysis of lipid droplets**
588 For lipid droplet analysis, the cells of interest were seeded on acid-washed coverslips in a 24-
589 well plate. Various treatments were performed as described in the figure legends. To stain for
590 lipid droplets, cells were washed with 1x PBS buffer and fixed in a solution containing 4%
591 paraformaldehyde (PFA) and 1x PBS for 10 minutes at room temperature. After fixing, cells
592 were washed 3 times with 1x PBS, and then cells were permeabilized with immunofluorescence
593 (IF) block buffer (1x PBS, 1% BSA and 0.1% Triton X-100, filter sterilized through a 0.2 μm filter)
594 for 15 minutes at room temperature. Cells were then incubated with 10 μM Bodipy 493/503
595 (Cayman Chemical; Cat# 25892) in IF block buffer for 1 hour followed by 3 washes with 1x PBS.
596 Coverslips were mounted on glass slides using ProLong Diamond Antifade Mountant (P36962,
597 Invitrogen/thermo fisher) and left to cure overnight at room temperature before imaging. Imaging
598 was conducted using a Keyence BZ-X800L fluorescence microscope.
599 To co-stain for proteins of interest (ACC1 or FASN) and lipid droplets, cells were treated
600 the same as above. After the 15 minute permeabilization step, cells were stained with ACC1
601 primary antibody (RRID: AB_2882621) diluted 1:1000 in IF block buffer for 1 hour at room
602 temperature. Coverslips were then washed 3x with IF block buffer before adding a mixture of 10
603 μM BODIPY 493/503 and secondary antibody (anti- mouse 647; RRID:AB_3073503) diluted

604 1:500 in IF block buffer for 1 hour. Alternatively (**Fig. 3c**), CoraLite Plus 647-conjugated ACC1
605 mouse polyclonal antibody (RRID: AB_11042445) was diluted 1:500 along with 10 μM BODIPY
606 493/503 in IF block buffer. After 1 hour of incubation, cells were washed 3x with IF block buffer,
607 and then mounted on glass slides and imaged as described above.
608
609 **Quantification of lipid droplets**
610 To quantify lipid droplets (LDs), images were processed using ImageJ software. First, images
611 were imported into ImageJ and then the images were converted to an 8-bit grayscale format.
612 Thresholding was performed to eliminate background by manually adjusting the threshold
613 intensity. Within a single experiment, all threshold values were kept constant for equal
614 comparisons of the images.
615 LDs were then quantified using the analyze particles function in ImageJ and the
616 parameters were configured to limit particle size to a minimum of 2 pixels² to eliminate very
617 small thresholded noise; circularity was set to 0.00-1.00. The results window provided raw data,
618 including the LD area (pixels² was converted into μm² using the conversion factor for our
619 microscope = 0.12581 μm/ pixel), which was copied into excel for analysis. LDs per cell were
620 calculated by dividing the total number of LDs for a field from the total number of nuclei in a
621 given field. In Extended data Fig. 3e, LDs were counted manually and assigned to a specific cell
622 to get a measurement of per-cell LD numbers. This latter method was not a preferred method
623 because when cells reach >70% confluency, it is often difficult to ascertain which LD belongs to
624 which cell.
625
626 **Cellular fractionation to isolate lipid droplets**
627 HAP1 WT cells were seeded on two 15 cm plates, with one plate treated with 30 μM Firsocostat
628 for 16 hours. Cells were harvested by gentle scraping in ice cold 1x PBS. The cell suspensions
629 were then centrifuged at 1000 x*g* for 5 minutes at 4°C to obtain cell pellets. After removing the
630 supernatant the pellets were resuspended in 8% sucrose buffer containing 0.25 M sucrose, 50
631 mM Tris-HCl (pH 7.4), 150 mM NaCl, 1x Protease Inhibitor Cocktail, and 1x Phosphatase
632 Inhibitor (1 PhosSTOP tablet per 10 ml cell extract or buffer, Millipore Sigma Cat #
633 4906845001). After incubating for 10 minutes on ice, the cells were lysed by passage through a
634 chilled ball-bearing cell homogenizer (isobiotec) with a 12 μm clearance 8 times. Successful
635 lysis was confirmed using Trypan blue staining (Gibco, Cat#15250061). A fraction (~50 μL) of
636 the homogenate was saved for Western blotting (whole-cell lysate). The remainder of the
637 homogenate was centrifuged twice at 1000 x*g* for 10 minutes each to pellet nuclei. The
638 supernatant (~600 μL from the top) was pipetted into a separate chilled microtube and the
639 pelleted nuclei was saved for Western blotting.
640 To isolate lipid droplets (LDs), 600 μL of 0% sucrose buffer (150 mM NaCl and 50 mM
641 Tris-HCl pH 7.4) was slowly added on top of the supernatant isolated above while trying to
642 maintain the separation of different sucrose densities. The tubes were centrifuged at 130,000 x*g*
643 for 1 hour at 4°C. LDs were collected in four, 50 μL fractions (total volume 200 μL) using a pre-
644 wetted pipette tip starting from the top floating layer, which appeared cloudy. The remaining
645 ~400 μL of 0% sucrose buffer was removed. The bottom ~600 uL cytoplasmic fraction was
646 collected and saved for Western blotting. Finally, the pelleted plasma membrane fraction was
647 resuspended in Lysis Buffer (10% glycerol, 2x Protease Inhibitor Cocktail (S8830, Millipore

648 sigma), 150 mM NaCl, 50 mM tris-HCl (pH 8), 1% NP-40 and 1 mM $MgCl_2$) and saved for
649 Western blotting.
650 The four LD fractions were washed with 500 µL 0% sucrose buffer by spinning at 20,000
651 x*g* for 30 minutes at 4°C. Next using a syringe needle, ~600 µL from the bottom of the tube was
652 removed and the top portion was saved for Western blotting of the LD fraction.
653 For Western blot analysis, the whole cell fraction was lysed by adding NP-40 to 1%. The
654 nuclear fraction was also resuspended in Lysis Buffer. The whole cell, nuclear, and plasma
655 membrane fractions were mechanically shaken at 4°C for 45 minutes to aid in lysis. The lysates
656 were then clarified by spinning at 18,000 x*g* for 30 minutes to remove aggregated material and
657 DNA. Finally, protein concentrations for the whole cell, nucleus, cytoplasm and plasma
658 membrane fractions were measured with a BCA assay, and equal amounts of protein were
659 saved for Western blots. LD fractions were also lysed by adding 1% NP-40, but BCA assays
660 revealed very low protein concentrations. For Western blot, the ~40 µL (a maximum possible
661 volume) of lysed LDs were loaded.
662
663 **Western blotting**
664 Cells were plated on a 6 cm dish and treated with small molecules when indicated. In **Fig. 6a**,
665 primary hepatocytes were isolated from 8-week old mice and then plated on collagen-coated
666 coverslips prior to analysis. Cells were then washed and scraped with chilled 1x PBS, and then
667 pelleted by spinning at 1000 x*g* for 5 minutes at 4°C. After removing the supernatant, the cells
668 were lysed with Lysis Buffer (10% glycerol, 2x Protease Inhibitor Cocktail (S8830, Millipore
669 sigma), 150 mM NaCl, 50 mM tris-HCl (pH 8), 1% NP-40 and 1 mM $MgCl_2$) at 4°C using a
670 mechanical shaker for 1 hour. Lysates were spun for 30 minutes at 18,000 x*g* and 4°C, and then
671 supernatants were transferred to a new tube. A BCA assay was performed on the supernatant to
672 determine the total protein concentration. Samples containing equal amounts of protein (~40 µg
673 per well) in 1X mPAGE LDS Sample Buffer (MPSB, millipore sigma) and 100 mM Dithiothreitol
674 (BP17225, Fisher) were incubated at 37 °C for 30 minutes before SDS-PAGE.
675 After completion of the SDS-PAGE, samples were transferred from the gel to a PVDF
676 membrane (IPVH85R, millipore sigma). The bands were cut after staining the membrane with
677 Ponceau stain and blocked with 5% nonfat milk in TBST (1x TBS, 10% tween). For analysis of
678 knockout cell lines, the membranes were incubated with the appropriate dilutions of
679 commercially available primary antibodies (ACAT1, ACC1, NPC1, FASN, ATGL) in 5% nonfat
680 milk diluted in TBST for 2 hours at room temperature, washed 3 times with TBST for 5 minutes
681 each, and then incubated with HRP-conjugated secondary antibodies diluted to 1:10,000 for 1
682 hour at room temperature. After washing the membrane three times with TBST for 5 minutes
683 each the blot was developed using ECL solutions (PI32209, Fisher/ Pierce).
684
685 **Generation of HAP1 mutant cell library for random insertion mutagenesis screen**
686 To randomly mutate the genome we used a retrovirus bearing a Gene Trap (GT) cassette that
687 introduces a splice acceptor site and a poly A tail, which terminates transcription regardless of
688 whether it inserts into introns or exons [84]. In contrast to CRISPR knockout screens, GT
689 mutagenesis can identify regulatory mechanisms that originate in non-coding regions like
690 promoters, and it can identify hypomorphic and dominant negative alleles by truncating proteins.

691 The production of GT virus was previously reported[85]. Briefly, to produce GT retrovirus,
692 15 million HEK 293FT cells were seeded into six T-175 flasks in 10% FBS DMEM media lacking
693 antibiotics. When cells reached 80% confluency, they were transected with two retroviral
694 transfer plasmids containing the GT in two reading frames (3.3 µg pGT-mCherry and 3.3 µg pG-
695 +1-mCherry), a plasmid with viral packaging genes (4 µg of pCMV-Gag-Pol), a plasmid with viral
696 envelope genes (2.6 µg of pCMV-VSV-G), and a plasmid that enhances translation (1.7 µg of
697 pAdVAntage). First, 45 µL of X-tremeGENE HP was added to 450 µL of OptiMEM for 5 minutes
698 at room temperature, and then plasmids were added to the mixture, which was briefly vortexed
699 and then incubated for 30 minutes at room temperature. The transfection reaction was added
700 dropwise to the 293FT cells. After 16 hours, virus-containing media was harvested, filtered
701 through a 0.45 µm low-protein binding filter and then concentrated by ultracentrifugation at
702 65,000 x*g* and 4°C for 1.5 hours in a swinging bucket rotor. Eight hours later, the virus was
703 harvested and concentrated for a second time. After centrifugation, the supernatant was
704 removed, leaving ~ 1 mL of media to avoid disrupting the viral pellet. Tubes were then sealed
705 with parafilm and incubated overnight at 4°C.
706 To generate the HAP1 cell library WT HAP1 cells were pre-sorted for haploidy using a
707 Hoechst stain. Then, 20 million haploid HAP1 cells were seeded into each of three T-175 flasks
708 in antibiotic free 10% FBS IMDM. Immediately before infecting with GT-bearing retrovirus, the
709 viral pellets were combined and resuspended in 76 mL of antibiotic free 10% FBS IMDM
710 containing 4 µg/mL polybrene. One-third of this mixture was added to each of the three flasks
711 containing WT HAP1 cells. Cells were expanded and maintained in multiple flasks, such that 50-
712 100 million cells were kept in passage at any given time to ensure the genotypic richness of the
713 library was maintained. Flow cytometry analysis measuring the GT-based mCherry fluorescence
714 was used to assess transduction efficiency, which was determined to be >90%.
715
716 **Random insertion mutagenesis screens**
717 For each screen, 20 million HAP1-GT cells were seeded in 7x T-175 flasks in 10% FBS IMDM
718 media. To find genes that increase PM cholesterol after NPC1 loss of function, all 7 flasks were
719 treated 8 hours after seeding with 1 µM U18666A. 20 hours later, 1 flask of cells was harvested
720 by trypsinization, pelleted at 1000 x*g*, and then snap frozen as an unsorted control. The
721 remaining flasks were prepared for Fluorescence Activated Cell Sorting (FACS). Plates were
722 processed one at a time, one per hour. After washing with 1x PBS, cells were trypsinized and
723 then spun at 1000 x*g* to isolate a cell pellet. Cells were then resuspended in 4 µM mNG-ALOD4
724 diluted into ice cold Probe Block Buffer (1x PBS, 1% BSA, filter sterilized). After 20 minutes of
725 staining on ice, cells with the top 10% of mNG-ALOD4 fluorescence were isolated with FACS.
726 Approximately 1-2 million cells were harvested per T-175 flask. After FACS, cells were spun
727 down and then seeded into the same 15 cm plate. Cells were then expanded until 6x T-175
728 flasks could be reseeded. FACS was carried out 2 consecutive times to enrich the cells with
729 high mNG-ALOD4 fluorescence. After the second sort, 30 million cells were pelleted and snap
730 frozen in liquid nitrogen. Library preparation and the computational analysis that follows has
731 been previously described in detail [86]. The only difference is that for the calculation of FDR-
732 corrected *p*-values (**Fig. 1g**, **h**) we included all GT insertions, regardless of orientation, for both
733 the selected and unsorted cell populations.

To identify genes that regulate cholesterol trafficking in response to 25-hydroxycholesterol, 20 million HAP1-GT cells were seeded in 7x T-175 flasks in 10% FBS IMDM, as described above. On the day of FACS sorting, one plate was isolated as the unsorted control. The remaining 6 plates were treated in a staggered manner, with 1 flask treated every hour with 4 μM 25-hydroxycholesterol. Each total treatment time was 6 hours. After 6 hours of treatment, cells were harvested by trypsinization, pelleted, and then isolated using the same protocol described above. For this screen, cells were sorted a total of three times, which may give rise to the increased FDR-corrected p-values observed for this screen compared to the U18666A screen (**Fig. 1g**, **h**).

Mass spectrometry analysis of lipid species

WT HAP1 cells were grown on 4x 15 cm dishes per treatment condition until ~75% confluent in 5% FBS IMDM. Cells were then moved into 5% LDS media with or without inhibitor (30 μM Firsocostat) for 24 hours. Media was removed and cells were washed gently 3x with room temperature 1x PBS to remove dead cell debris. Cells were then scraped in ice cold 1x PBS on an ice metal rack in the tissue culture hood. Each plate of cells was moved to a single 15 mL conical tube and then spun at 1000 x*g* to pellet. PBS was then aspirated, cells were snap frozen in liquid nitrogen and shipped on dry ice to Metabolon Inc. for analysis.

Raw values obtained from Metabolon Inc. are areas under the curve for each detected lipid species, normalized to protein concentrations for each sample. Values are not exact quantitative measurements since internal standards were not used. All comparisons made should only be considered as relative changes compared to the control sample (5% LDS lacking inhibitors).

For analysis of lipids from *Acc1/Acc2* flox/flox mice and Albumin-CRE *Acc1/Acc2* flox/flox mice, mice were chow-fed, with n=4 per group. Lipids were extracted by liquid-liquid extraction and analyzed by LC-MS/MS using internal standards. Each value was normalized to tissue weight.

Measurements of the rate of fatty acid and cholesterol synthesis in mouse livers

For analysis of fatty acid synthesis rates, mice were maintained on a chow diet and subjected to a time-restricted feeding regimen (feeding from 6 PM to 6 AM; fasting from 6 AM to 6 PM) for 3 consecutive days prior to the assay. $[^3H]H_2O$ (50 mCi) was administered intraperitoneally, and hepatic fatty acid synthesis rates were determined by quantifying ^3H incorporation into newly synthesized fatty acids, as previously described [87]. Hepatic sterol synthesis rates were assessed by measuring $[^3H]$ incorporation into newly synthesized sterols, as previously described [87].

Measurement of total liver cholesterol and fecal cholesterol content in mice

For hepatic liver cholesterol measurements, approximately 100 mg of liver tissue was used for lipid extraction, and cholesterol quantification was measured using the Infinity™ Cholesterol Liquid Stable Reagent.

For fecal cholesterol measurements, feces were collected from mice (n = 7 per group), which were individually housed overnight. Around 100 mg of feces was homogenized in Folch reagent (chloroform:methanol, 2:1), and the organic phase was extracted by phase separation

with saline and isolated by centrifugation. A portion of the organic phase was dried in the presence of Triton X-100, and cholesterol content was measured using the Infinity™ Cholesterol Liquid Stable Reagent.

RNA sequencing analysis

WT HAP1 cells were grown in 6-well plates, with 4 wells per condition, until ~75% confluent in 5% FBS IMDM. Cells were then moved into 5% LDS media for 16 hours. Cells were then treated with or without 10 μM Lovastatin, 30 μM Firsocostat, 5 μM Triacsin-C or 10 μM C75 for 6 hours. Cells were then washed twice with 1x PBS, and then all PBS was aspirated.

RNA was isolated using Trizol-chloroform extraction. Briefly, 800 μL Trizol was added directly to the wells, incubated for 5 minutes, and then transferred to DNase/RNase-free 1.5 mL eppendorf tubes. After adding 160 μL chloroform, samples were shaken vigorously for 15 seconds and incubated at room temperature for 3 minutes. Phase separation was achieved by centrifugation at 12,000 x*g* for 15 minutes at 4 °C, and then the aqueous phase was transferred to a new tube. Next, 400 μL isopropanol was added and then samples were incubated for 10 minutes at room temperature. RNA was then pelleted by centrifugation at 12,000 x*g* for 10 minutes at 4 °C. The RNA pellet was washed with 800 μL 75% ethanol, vortexed briefly, and centrifuged at 7,500 x*g* for 5 minutes at 4 °C. The supernatant was removed, and pellets were spun again for 5 minutes. Residual ethanol was removed and pellets were air-dried at room temperature for 5–10 minutes until the pellet turned translucent. RNA was resuspended in 40 μL DNase/RNase-free water, incubated at room temperature for 10 minutes, and gently mixed. RNA was stored at -80 °C and shipped to Novogene USA Inc. for standard RNA sequencing analysis. The returned FASTQ files were analyzed using the PartekFlow software using previously described methods from Xiaowen Wang (Field Application Specialist from Partek Incorporated). Data was processed using a differential gene set enrichment analysis (DeSeq2).

The bubble plots (**Fig. 6g**, **h**) were generated using both GraphPad Prism 10 and Adobe Illustrator. First, a list of genes of interest were curated for SREBP2 (**Fig. 6g**) and SREBP1 (**Fig. 6h**). SREBP1 targets were found using a publically available ChIP-Seq database (ChIP-Atlas). Next, FDR-corrected *p*-values were -Log_{10} transformed, and Log_2 fold changes values were subjected to exponential transformation (2^(Log_2(fold-change values)). The transformed *p*-values and fold change values for genes of interest were found for each treatment and given a unique identifier (e.g. HMGCRi-ACAT2, ACC1i-ACAT2, ACSLi-ACAT2, and FASNi-ACAT). All genes were then plotted into one column using a Multiple Variable analysis plot type in Graph Pad Prism 10. Bubble size was set to be determined by the transformed *p*-value, and bubble color was set to be the fold change; this software also assigned x-axis and y-axis positioning for the bubbles, however these were not used in the final figure generation. GraphPad Prism 10 was simply used to generate bubbles of meaningful size and color for each gene in its respective treatment. Finally, the GraphPad Prism 10 file was exported as a .emf file, opened in Adobe Illustrator, and the bubbles were re-arranged into a column graph.

Gene Set Enrichment Analysis

To analyze the top pathways affected by ACC1, ACSL, FASN, and HMGCR inhibition, we utilized the Gene Set Enrichment Analysis (GSEA) website. First, we navigated to the Explore

822 the Molecular Signatures Database (MSigDB), and then to the “Investigate” tab in the Human
823 Collections. In the “Input Gene Identifiers” box, we pasted the top 200 genes that were
824 differentially regulated for each treatment- rankings were made by sorting based on FDR-
825 corrected *p*-values. In the Compute Overlaps window, we selected the WikiPathways gene sets,
826 and then computed the overlaps. This returned the top 10 WikiPathways for each set of genes.
827 Enterocyte Cholesterol Metabolism (WP5333), Cholesterol Metabolism (WP5304), Cholesterol
828 Biosynthesis Pathway (WP197), and Cholesterol Biosynthesis Pathway in Hepatocytes
829 (WP5329) were excluded from the final plot due to their significant overlap with the genes found
830 in Cholesterol Metabolism with Bloch and Kandutsch-Russell Pathways (WP4718) and
831 Cholesterol Synthesis Disorders (WP5193), which were used in the final plot. If a pathway was
832 not found in the top 10 pathways identified, it was denoted in the plot as “nf” for not found.
833
834 **Crispr Cas9 mediated knockout of genes**
835 Two single guide RNA (sgRNA) sequences were designed using the Benchling software to
836 direct Cas9 binding and cleavage at two separate genomic sites[88]. Next the sgRNA guide
837 sequences were cloned into px458-GFP and px458-mCherry plasmids. The sequence verified
838 plasmids were next transfected into HAP1 cells and after 24 hours both mCherry- and GFP-
839 positive cells were single cell sorted into a 96 well plate using FACS. Subsequently, these
840 single-cell clones were expanded and then genotyped in order to identify knockouts.
841
842 **Statistical analysis**
843 Data analysis was done using GraphPad Prism 10.3.1. All statistical comparisons between two
844 datasets were conducted using a Student’s t-test with Welch’s correction. Ordinary one-way
845 ANOVA was applied when comparing one dataset to multiple others. P-values from GraphPad
846 Prism 10.4.1 are presented on the graphs using the following notation: not significant (ns) $p>$
847 0.1234, *$p\leq0.0332$, **$p\leq0.0021$, ***$p\leq0.0002$, and ****$p<0.0001$. Unless stated otherwise, all
848 experiments were repeated three times.
849
850 Figure 1 statistics: *p*-values: **a**, WT vs *GRAMD1* TKO $p<0.0001$; **b**, WT vs *GRAMD1* TKO (2 hr
851 25HC) $p=0.8044$, WT vs *GRAMD1* TKO (4 hr 25HC) $p=0.5201$, and WT vs *GRAMD1* TKO (6 hr
852 25HC) $p=0.2595$; **c**, Control vs LXR inhibitor $p=0.0468$; **d**, Control vs LXR inhibitor (2 hr 25HC)
853 $p=0.2070$, Control vs LXR inhibitor (4 hr 25HC) $p=0.0667$ and Control vs LXR inhibitor (6 hr
854 25HC) $p=0.0233$; **i**, WT vs NPC1i $p=0.0160$ and WT vs *ACC1* KO (NPC1i) $p=0.0608$; **j**, WT vs
855 *NPC1* KO $p=0.0124$ **k**, WT vs *ACC1* KO (3 hr 25HC) $p=0.0022$, WT vs *ACC1* KO (4.5 hr 25HC)
856 $p=0.0006$ and WT vs *ACC1* KO (6 hr 25HC) $p<0.0001$; **l** Control vs ACC1i (3 hr 25HC)
857 $p=0.0552$, Control vs ACC1i (4.5 hr 25HC) $p=0.0236$ and Control vs ACC1i (6 hr 25HC)
858 $p=0.0087$; **m**, 3T3 control vs ACC1i (3 hr 25HC) $p=0.0097$, 3T3 control vs ACC1i (4.5 hr 25HC)
859 $p=0.0069$ and 3T3 control vs ACC1i (6 hr 25HC) $p=0.0222$, 293T control vs ACC1i (3 hr 25HC)
860 $p=0.1192$, 293T control vs ACC1i (4.5 hr 25HC) $p=0.0452$ and 293T control vs ACC1i (6 hr
861 25HC) $p=0.0208$.
862
863 Figure 2 statistics: *p*-values are: **b**, WT vs *ACC1* KO $p<0.0001$; **c,** WT HAP1 untreated vs ACC1i
864 $p<0.0001$, 293T untreated vs ACC1i $p<0.0001$ and 3T3 untreated vs ACC1i $p<0.0001$; **d**,
865 untreated vs CP-640186 $p<0.0001$, untreated vs Firsocostat $p<0.0001$; **e**, WT vs KO (0.2

μg/mL) p=0.1871, WT vs KO (0.5 μg/mL) p=0.1171, WT vs KO (1.3 μg/mL) p=0.0024, WT vs KO (3.2 μg/mL) p=0.0056, WT vs KO (8 μg/mL) p=0.0344 and WT vs KO (20 μg/mL) p=0.7060; **h**, WT untreated vs 25HC p=0.0061 and *ACAT1/2* DKO untreated vs 25HC p=0.5563; **i**, WT vs *ACAT1/2* DKO (3 hr 25HC) p=0.1164, WT vs *ACAT1/2* DKO (4.5 hr 25HC) p=0.0176 and WT vs *ACAT1/2* DKO (6 hr 25HC) p=0.0001; **j**, *ACAT1/2* DKO control vs *ACAT1/2* DKO + ACC1i (2 hr 25HC) p=0.0012, *ACAT1/2* DKO control vs *ACAT1/2* DKO + ACC1i (4 hr 25HC) p=0.0003, and *ACAT1/2* DKO control vs *ACAT1/2* DKO + ACC1i (6 hr 25HC) p=0.0016; **l**, *ACAT1/2* DKO vs *ACC1/ACAT1/2* TKO (3 hr 25HC) p<0.0001, *ACAT1/2 DKO* vs *ACC1/ACAT1/2* TKO (4.5 hr 25HC) p<0.0001 and *ACAT1/2* DKO vs *ACC1/ACAT1/2* TKO (6 hr 25HC) p<0.0001; **m**, WT untreated vs *ACAT1/2* DKO untreated p=0.8348, *ACAT1/2* DKO vs *ACAT1/2* DKO + ACC1i p<0.0001; **n**, WT untreated vs 25HC p<0.0001, ACC1 KO untreated vs 25HC p=0.6349.

Figure 3 statistics: p-values are: **a**, WT 0 hr vs 3hr ACC1i p=0.0005, WT 0 hr vs 6hr ACC1i p<0.0001, WT 0 hr vs 24hr ACC1i p<0.0001, and WT HAP1 0 hr vs 48hr ACC1i p<0.0001; **h**, WT control vs ACSLi (2 hr 25HC) p=0.0116, WT control vs ACSLi (4 hr 25HC) p=0.0015 and WT control vs ACSLi (6 hr 25HC) p=0.0077; **i**, WT control vs ACSLi (2 hr ACC1i) p=0.0565, WT control vs ACSLi (4 hr ACC1i) p=0.0294 and WT control vs ACSLi (6 hr ACC1i) p=0.0273; **j,** control untreated vs oleic acid p=0.0050, ACC1i vs ACC1i + oleic acid p=0.0006, and ACSLi vs ACSLi + oleic acid p=0.0502 and **k**, control untreated vs oleic acid p=0.9312, ACC1i vs ACC1i + oleic acid p=0.0006, and ACSLi vs ACSLi + oleic acid p=0.0278.

Figure 4 statistics: p-values are: **c**, WT vs *ATGL* KO p= 0.1690; **d**, WT vs *ATGL* KO p<0.0001; **f**, WT untreated vs ACC1i p=0.0362 and *ATGL* KO untreated vs ACC1i p= 0.6774; **g**, WT vs *ATGL* KO (2 hr ACC1i) p= 0.1746, WT vs *ATGL* KO (4 hr ACC1i) p= 0.0511 and WT vs *ATGL* KO (6 hr ACC1i) p= 0.0121; and **h**, control vs ATGLi (2 hr ACC1i) p=0.0257, control vs ATGLi (4hr ACC1i) p=0.0079 and control vs ATGLi (6hr ACC1i) p=0.0138.

Figure 5 statistics: p-values are: **b**, untreated vs ACSLi p<0.0001, untreated vs ATGLi p<0.0001, ATGLi vs ATGLi + ACSLi p<0.0001; **c**, untreated vs ACSLi p<0.0001, untreated vs ATGLi p=0.0011, and ATGLi vs ATGLi + ACSLi p<0.0001; **g**, untreated vs ACC1i p<0.0001, untreated vs AMPKi p<0.0001, and AMPKi vs ACC1i + AMPKi p<0.0001; **h**, untreated vs ACC1i p<0.0001, untreated vs AMPKi p=0.0005, and AMPKi vs ACC1i + AMPKi p<0.0001; **i**, *ACAT1/2* DKO untreated vs ACC1i p<0.0001, *ACAT1/2* DKO untreated vs AMPKi p<0.0001, and *ACAT1/2* DKO AMPKi vs ACC1i+ AMPKi p<0.0001; **j**, *ACAT1/2* DKO untreated vs ACC1i p<0.0001, *ACAT1/2* DKO untreated vs AMPKi p<0.0001, and *ACAT1/2* DKO AMPKi vs ACC1i + AMPKi p<0.0001.

Figure 6 statistics: p-values are: **b**, WT vs *Acc* dLKO p<0.0001; **c**, WT vs *Acc* dLKO p=0.0022; **d**, WT vs *Acc* dLKO p=0.0005; **f**, WT vs *Acc* dLKO p=*0.0004*; **j**, WT vs *Acc* dLKO p<0.0001; **k**, WT vs *Acc* dLKO p=0.1915 and **l**, WT vs *Acc* dLKO p=0.0434.

References

1. Kumar, G. A., Jafurulla, M. & Chattopadhyay, A. The membrane as the gatekeeper of

908 infection: Cholesterol in host-pathogen interaction. *Chem. Phys. Lipids* **199**, 179–185
909 (2016).
910 2. Goluszko, P. & Nowicki, B. Membrane cholesterol: a crucial molecule affecting interactions
911 of microbial pathogens with mammalian cells. *Infect. Immun.* **73**, 7791–7796 (2005).
912 3. Radhakrishnan, A., Rohatgi, R. & Siebold, C. Cholesterol access in cellular membranes
913 controls Hedgehog signaling. *Nat. Chem. Biol.* **16**, 1303–1313 (2020).
914 4. Hussain, G. *et al.* Role of cholesterol and sphingolipids in brain development and
915 neurological diseases. *Lipids Health Dis.* **18**, 26 (2019).
916 5. Lönnfors, M., Doux, J. P. F., Killian, J. A., Nyholm, T. K. M. & Slotte, J. P. Sterols have
917 higher affinity for sphingomyelin than for phosphatidylcholine bilayers even at equal acyl-
918 chain order. *Biophys. J.* **100**, 2633–2641 (2011).
919 6. Demel, R. A., Jansen, J. W., van Dijck, P. W. & van Deenen, L. L. The preferential
920 interaction of cholesterol with different classes of phospholipids. *Biochim. Biophys. Acta*
921 **465**, 1–10 (1977).
922 7. Slotte, J. P. & Bierman, E. L. Depletion of plasma-membrane sphingomyelin rapidly alters
923 the distribution of cholesterol between plasma membranes and intracellular cholesterol
924 pools in cultured fibroblasts. *Biochem. J* **250**, 653–658 (1988).
925 8. Endapally, S. *et al.* Molecular Discrimination between Two Conformations of Sphingomyelin
926 in Plasma Membranes. *Cell* **176**, 1040–1053.e17 (2019).
927 9. Kinnebrew, M. *et al.* Cholesterol accessibility at the ciliary membrane controls hedgehog
928 signaling. *Elife* **8**, (2019).
929 10. Das, A., Brown, M. S., Anderson, D. D., Goldstein, J. L. & Radhakrishnan, A. Three pools of
930 plasma membrane cholesterol and their relation to cholesterol homeostasis. *Elife* **3**, (2014).
931 11. Infante, R. E. & Radhakrishnan, A. Continuous transport of a small fraction of plasma
932 membrane cholesterol to endoplasmic reticulum regulates total cellular cholesterol. *Elife* **6**,
933 (2017).
934 12. Radhakrishnan, A., Goldstein, J. L., McDonald, J. G. & Brown, M. S. Switch-like control of
935 SREBP-2 transport triggered by small changes in ER cholesterol: A delicate balance. *Cell*
936 *Metab.* **8**, 512–521 (2008).
937 13. Sun, L.-P., Seemann, J., Goldstein, J. L. & Brown, M. S. Sterol-regulated transport of
938 SREBPs from endoplasmic reticulum to Golgi: Insig renders sorting signal in Scap
939 inaccessible to COPII proteins. *Proc. Natl. Acad. Sci. U. S. A.* **104**, 6519–6526 (2007).
940 14. Brown, M. S. & Goldstein, J. L. Cholesterol feedback: from Schoenheimer's bottle to Scap's
941 MELADL. *J. Lipid Res.* **50 Suppl**, S15–27 (2009).
942 15. Brown, M. S. & Goldstein, J. L. The SREBP pathway: regulation of cholesterol metabolism
943 by proteolysis of a membrane-bound transcription factor. *Cell* **89**, 331–340 (1997).
944 16. Abrams, M. E. *et al.* Oxysterols provide innate immunity to bacterial infection by mobilizing
945 cell surface accessible cholesterol. *Nat. Microbiol.* **5**, 929–942 (2020).
946 17. Zhou, Q. D. *et al.* Interferon-mediated reprogramming of membrane cholesterol to evade
947 bacterial toxins. *Nat. Immunol.* **21**, 746–755 (2020).
948 18. Wang, S. *et al.* Cholesterol 25-Hydroxylase inhibits SARS-CoV-2 and other coronaviruses
949 by depleting membrane cholesterol. *EMBO J.* **39**, e106057 (2020).
950 19. Zhao, J., Chen, J., Li, M., Chen, M. & Sun, C. Multifaceted functions of CH25H and 25HC
951 to modulate the lipid metabolism, immune responses, and broadly antiviral activities.

Viruses **12**, (2020).
20. Heisler, D. B. *et al.* A concerted mechanism involving ACAT and SREBPs by which oxysterols deplete accessible cholesterol to restrict microbial infection. *Elife* **12**, (2023).
21. Lichtenstein, A. H. & Brecher, P. Esterification of cholesterol and 25-hydroxycholesterol by rat liver microsomes. *Biochim. Biophys. Acta* **751**, 340–348 (1983).
22. Lange, Y., Ye, J. & Strebel, F. Movement of 25-hydroxycholesterol from the plasma membrane to the rough endoplasmic reticulum in cultured hepatoma cells. *J. Lipid Res.* **36**, 1092–1097 (1995).
23. Liu, Y. *et al.* Activation of liver X receptor plays a central role in antiviral actions of 25-hydroxycholesterol. *J. Lipid Res.* **59**, 2287–2296 (2018).
24. Adams, C. M. *et al.* Cholesterol and 25-hydroxycholesterol inhibit activation of SREBPs by different mechanisms, both involving SCAP and Insigs. *J. Biol. Chem.* **279**, 52772–52780 (2004).
25. Goldstein, J. L., DeBose-Boyd, R. A. & Brown, M. S. Protein sensors for membrane sterols. *Cell* **124**, 35–46 (2006).
26. Venkateswaran, A. *et al.* Control of cellular cholesterol efflux by the nuclear oxysterol receptor LXR alpha. *Proc. Natl. Acad. Sci. U. S. A.* **97**, 12097–12102 (2000).
27. Wong, J., Quinn, C. & Brown, A. J. SREBP-2 positively regulates transcription of the cholesterol efflux gene, ABCA1, by generating oxysterol ligands for LXR. *Biochem. J.* **400**, 485–491 (2006).
28. Ercan, B., Naito, T., Koh, D. H. Z., Dharmawan, D. & Saheki, Y. Molecular basis of accessible plasma membrane cholesterol recognition by the GRAM domain of GRAMD1b. *EMBO J.* **40**, e106524 (2021).
29. Naito, T. & Saheki, Y. GRAMD1-mediated accessible cholesterol sensing and transport. *Biochim. Biophys. Acta Mol. Cell Biol. Lipids* **1866**, 158957 (2021).
30. Naito, T. *et al.* Regulation of cellular cholesterol distribution via non-vesicular lipid transport at ER-Golgi contact sites. *Nat. Commun.* **14**, 5867 (2023).
31. Ferrari, A. *et al.* Aster-dependent nonvesicular transport facilitates dietary cholesterol uptake. *Science* **382**, eadf0966 (2023).
32. Soccio, R. E. *et al.* The cholesterol-regulated StarD4 gene encodes a StAR-related lipid transfer protein with two closely related homologues, StarD5 and StarD6. *Proc. Natl. Acad. Sci. U. S. A.* **99**, 6943–6948 (2002).
33. Soccio, R. E. The STARD4 subfamily: STARD4 and STARD5 in cholesterol metabolism. in *Cholesterol Transporters of the START Domain Protein Family in Health and Disease* 139–171 (Springer New York, New York, NY, 2014).
34. Subtil, A. *et al.* Acute cholesterol depletion inhibits clathrin-coated pit budding. *Proc. Natl. Acad. Sci. U. S. A.* **96**, 6775–6780 (1999).
35. Lippincott-Schwartz, J. & Phair, R. D. Lipids and cholesterol as regulators of traffic in the endomembrane system. *Annu. Rev. Biophys.* **39**, 559–578 (2010).
36. Möbius, W. *et al.* Recycling compartments and the internal vesicles of multivesicular bodies harbor most of the cholesterol found in the endocytic pathway: Cholesterol in the endocytic pathway. *Traffic* **4**, 222–231 (2003).
37. Linder, M. D. *et al.* Rab8-dependent recycling promotes endosomal cholesterol removal in normal and sphingolipidosis cells. *Mol. Biol. Cell* **18**, 47–56 (2007).

38. Johnson, K. A. & Radhakrishnan, A. The use of anthrolysin O and ostreolysin A to study cholesterol in cell membranes. *Methods Enzymol.* **649**, 543–566 (2021).
39. Endapally, S., Infante, R. E. & Radhakrishnan, A. Monitoring and modulating intracellular cholesterol trafficking using ALOD4, a cholesterol-binding protein. *Methods Mol. Biol.* **1949**, 153–163 (2019).
40. Wakil, S. J. & Abu-Elheiga, L. A. Fatty acid metabolism: target for metabolic syndrome. *J. Lipid Res.* **50 Suppl**, S138–43 (2009).
41. Li, Q. *et al.* CircACC1 regulates assembly and activation of AMPK complex under metabolic stress. *Cell Metab.* **30**, 157–173.e7 (2019).
42. Lu, A. *et al.* CRISPR screens for lipid regulators reveal a role for ER-bound SNX13 in lysosomal cholesterol export. *J. Cell Biol.* **221**, (2022).
43. Russo, L. *et al.* Cholesterol 25-hydroxylase (CH25H) as a promoter of adipose tissue inflammation in obesity and diabetes. *Mol. Metab.* **39**, 100983 (2020).
44. Raselli, T. *et al.* The oxysterol synthesising enzyme CH25H contributes to the development of intestinal fibrosis. *J. Crohns. Colitis* **13**, 1186–1200 (2019).
45. Toral-Rios, D. *et al.* Cholesterol 25-hydroxylase mediates neuroinflammation and neurodegeneration in a mouse model of tauopathy. *J. Exp. Med.* **221**, (2024).
46. Nguyen, C., Saint-Pol, J., Dib, S., Pot, C. & Gosselet, F. 25-Hydroxycholesterol in health and diseases. *J. Lipid Res.* **65**, 100486 (2024).
47. Harriman, G. *et al.* Acetyl-CoA carboxylase inhibition by ND-630 reduces hepatic steatosis, improves insulin sensitivity, and modulates dyslipidemia in rats. *Proc. Natl. Acad. Sci. U. S. A.* **113**, E1796–805 (2016).
48. Luo, D.-X. *et al.* Targeting acetyl-CoA carboxylases: small molecular inhibitors and their therapeutic potential. *Recent Pat. Anticancer Drug Discov.* **7**, 168–184 (2012).
49. Zhang, H., Tweel, B., Li, J. & Tong, L. Crystal structure of the carboxyltransferase domain of acetyl-coenzyme A carboxylase in complex with CP-640186. *Structure* **12**, 1683–1691 (2004).
50. Das, A., Goldstein, J. L., Anderson, D. D., Brown, M. S. & Radhakrishnan, A. Use of mutant 125I-perfringolysin O to probe transport and organization of cholesterol in membranes of animal cells. *Proc. Natl. Acad. Sci. U. S. A.* **110**, 10580–10585 (2013).
51. Ross, A. C., Go, K. J., Heider, J. G. & Rothblat, G. H. Selective inhibition of acyl coenzyme A:cholesterol acyltransferase by compound 58-035. *J. Biol. Chem.* **259**, 815–819 (1984).
52. Liu, Y. *et al.* 25-Hydroxycholesterol activates the expression of cholesterol 25-hydroxylase in an LXR-dependent mechanism. *J. Lipid Res.* **59**, 439–451 (2018).
53. Alberts, A. Discovery, biochemistry and biology of lovastatin. *Am. J. Cardiol.* **62**, 10J–15J (1988).
54. Peterson, C. W. H., Deol, K. K., To, M. & Olzmann, J. A. Optimized protocol for the identification of lipid droplet proteomes using proximity labeling proteomics in cultured human cells. *STAR Protoc.* **2**, 100579 (2021).
55. Bersuker, K. *et al.* A proximity labeling strategy provides insights into the composition and dynamics of lipid droplet proteomes. *Dev. Cell* **44**, 97–112.e7 (2018).
56. Bacci, M. *et al.* Acetyl-CoA carboxylase 1 controls a lipid droplet-peroxisome axis and is a vulnerability of endocrine-resistant ER+ breast cancer. *Sci. Transl. Med.* **16**, eadf9874 (2024).

1040 57. Hsieh, K. *et al.* Perilipin family members preferentially sequester to either triacylglycerol-
1041 specific or cholesteryl-ester-specific intracellular lipid storage droplets. *J. Cell Sci.* **125**,
1042 4067–4076 (2012).
1043 58. Dumesnil, C. *et al.* Cholesterol esters form supercooled lipid droplets whose nucleation is
1044 facilitated by triacylglycerols. *Nat. Commun.* **14**, 915 (2023).
1045 59. Majchrzak, M. *et al.* Perilipin membrane integration determines lipid droplet heterogeneity in
1046 differentiating adipocytes. *Cell Rep.* **43**, 114093 (2024).
1047 60. Ahmadian, M. *et al.* Desnutrin/ATGL is regulated by AMPK and is required for a brown
1048 adipose phenotype. *Cell Metab.* **13**, 739–748 (2011).
1049 61. Mathiowetz, A. J. *et al.* CLCC1 promotes hepatic neutral lipid flux and nuclear pore complex
1050 assembly. *bioRxivorg* (2024) doi:10.1101/2024.06.07.597858.
1051 62. Roberts, M. A. *et al.* Parallel CRISPR-Cas9 screens identify mechanisms of PLIN2 and lipid
1052 droplet regulation. *Dev. Cell* **58**, 1782–1800.e10 (2023).
1053 63. Zimmermann, R. *et al.* Fat mobilization in adipose tissue is promoted by adipose
1054 triglyceride lipase. *Science* **306**, 1383–1386 (2004).
1055 64. Grabner, G. F. *et al.* Small-molecule inhibitors targeting lipolysis in human adipocytes. *J.*
1056 *Am. Chem. Soc.* **144**, 6237–6250 (2022).
1057 65. Fang, C. *et al.* The AMPK pathway in fatty liver disease. *Front. Physiol.* **13**, 970292 (2022).
1058 66. Hardie, D. G., Schaffer, B. E. & Brunet, A. AMPK: An energy-sensing pathway with multiple
1059 inputs and outputs. *Trends Cell Biol.* **26**, 190–201 (2016).
1060 67. Zhou, G. *et al.* Role of AMP-activated protein kinase in mechanism of metformin action. *J.*
1061 *Clin. Invest.* **108**, 1167–1174 (2001).
1062 68. Kim, C.-W. *et al.* Acetyl CoA carboxylase inhibition reduces hepatic steatosis but elevates
1063 plasma triglycerides in mice and humans: A bedside to bench investigation. *Cell Metab.* **26**,
1064 394–406.e6 (2017).
1065 69. Schwarz, M., Russell, D. W., Dietschy, J. M. & Turley, S. D. Marked reduction in bile acid
1066 synthesis in cholesterol 7α-hydroxylase-deficient mice does not lead to diminished tissue
1067 cholesterol turnover or to hypercholesterolemia. *J. Lipid Res.* **39**, 1833–1843 (1998).
1068 70. Gruffat, D., Durand, D., Graulet, B. & Bauchart, D. Regulation of VLDL synthesis and
1069 secretion in the liver. *Reproduction Nutrition Development* **36**, 375–389 (1996).
1070 71. Brown, M. S., Radhakrishnan, A. & Goldstein, J. L. Retrospective on cholesterol
1071 homeostasis: The central role of Scap. *Annu. Rev. Biochem.* **87**, 783–807 (2018).
1072 72. Edwards, P. A., Tabor, D., Kast, H. R. & Venkateswaran, A. Regulation of gene expression
1073 by SREBP and SCAP. *Biochim. Biophys. Acta* **1529**, 103–113 (2000).
1074 73. Kim, J. B. *et al.* Nutritional and insulin regulation of fatty acid synthetase and leptin gene
1075 expression through ADD1/SREBP1. *J. Clin. Invest.* **101**, 1–9 (1998).
1076 74. Zhang, Y., Yin, L. & Hillgartner, F. B. SREBP-1 integrates the actions of thyroid hormone,
1077 insulin, cAMP, and medium-chain fatty acids on ACCalpha transcription in hepatocytes. *J.*
1078 *Lipid Res.* **44**, 356–368 (2003).
1079 75. Kim, H.-J., Miyazaki, M. & Ntambi, J. M. Dietary cholesterol opposes PUFA-mediated
1080 repression of the stearoyl-CoA desaturase-1 gene by SREBP-1 independent mechanism. *J.*
1081 *Lipid Res.* **43**, 1750–1757 (2002).
1082 76. Sekiya, M. *et al.* Polyunsaturated fatty acids ameliorate hepatic steatosis in obese mice by
1083 SREBP-1 suppression. *Hepatology* **38**, (2003).

77. Walther, T. C. & Farese, R. V., Jr. Lipid droplets and cellular lipid metabolism. *Annu. Rev. Biochem.* **81**, 687–714 (2012).
78. Olzmann, J. A. & Carvalho, P. Dynamics and functions of lipid droplets. *Nat. Rev. Mol. Cell Biol.* **20**, 137–155 (2019).
79. Naito, T. *et al.* Movement of accessible plasma membrane cholesterol by the GRAMD1 lipid transfer protein complex. *Elife* **8**, (2019).
80. Peng, W. *et al.* Endosomal trafficking participates in lipid droplet catabolism to maintain lipid homeostasis. *Nat. Commun.* **16**, 1917 (2025).
81. Forwell, A. L. *et al.* Analysis of CH25H in multiple sclerosis and neuromyelitis optica. *J. Neuroimmunol.* **291**, 70–72 (2016).
82. Haney, M. S. *et al.* APOE4/4 is linked to damaging lipid droplets in Alzheimer's disease microglia. *Nature* **628**, 154–161 (2024).
83. Zadoorian, A., Du, X. & Yang, H. Lipid droplet biogenesis and functions in health and disease. *Nat. Rev. Endocrinol.* **19**, 443–459 (2023).
84. Carette, J. E. *et al.* Haploid genetic screens in human cells identify host factors used by pathogens. *Science* **326**, 1231–1235 (2009).
85. Khandwala, C. B. *et al.* Direct ionic stress sensing and mitigation by the transcription factor NFAT5. *bioRxivorg* (2023) doi:10.1101/2023.09.23.559074.
86. Lebensohn, A. M. *et al.* Comparative genetic screens in human cells reveal new regulatory mechanisms in WNT signaling. *Elife* **5**, (2016).
87. Shimano, H. *et al.* Overproduction of cholesterol and fatty acids causes massive liver enlargement in transgenic mice expressing truncated SREBP-1a. *J. Clin. Invest.* **98**, 1575–1584 (1996).
88. Ran, F. A. *et al.* Genome engineering using the CRISPR-Cas9 system. *Nat. Protoc.* **8**, 2281–2308 (2013).
89. Ikonen, E. & Zhou, X. Cholesterol transport between cellular membranes: A balancing act between interconnected lipid fluxes. *Dev. Cell* **56**, 1430–1436 (2021).
90. Zhou, F. *et al.* Filament structures unveil the dynamic organization of human acetyl-CoA carboxylase. *Sci. Adv.* **10**, eado4880 (2024).
91. Hunkeler, M. *et al.* Structural basis for regulation of human acetyl-CoA carboxylase. *Nature* **558**, 470–474 (2018).

1123

Extended data Fig. 1

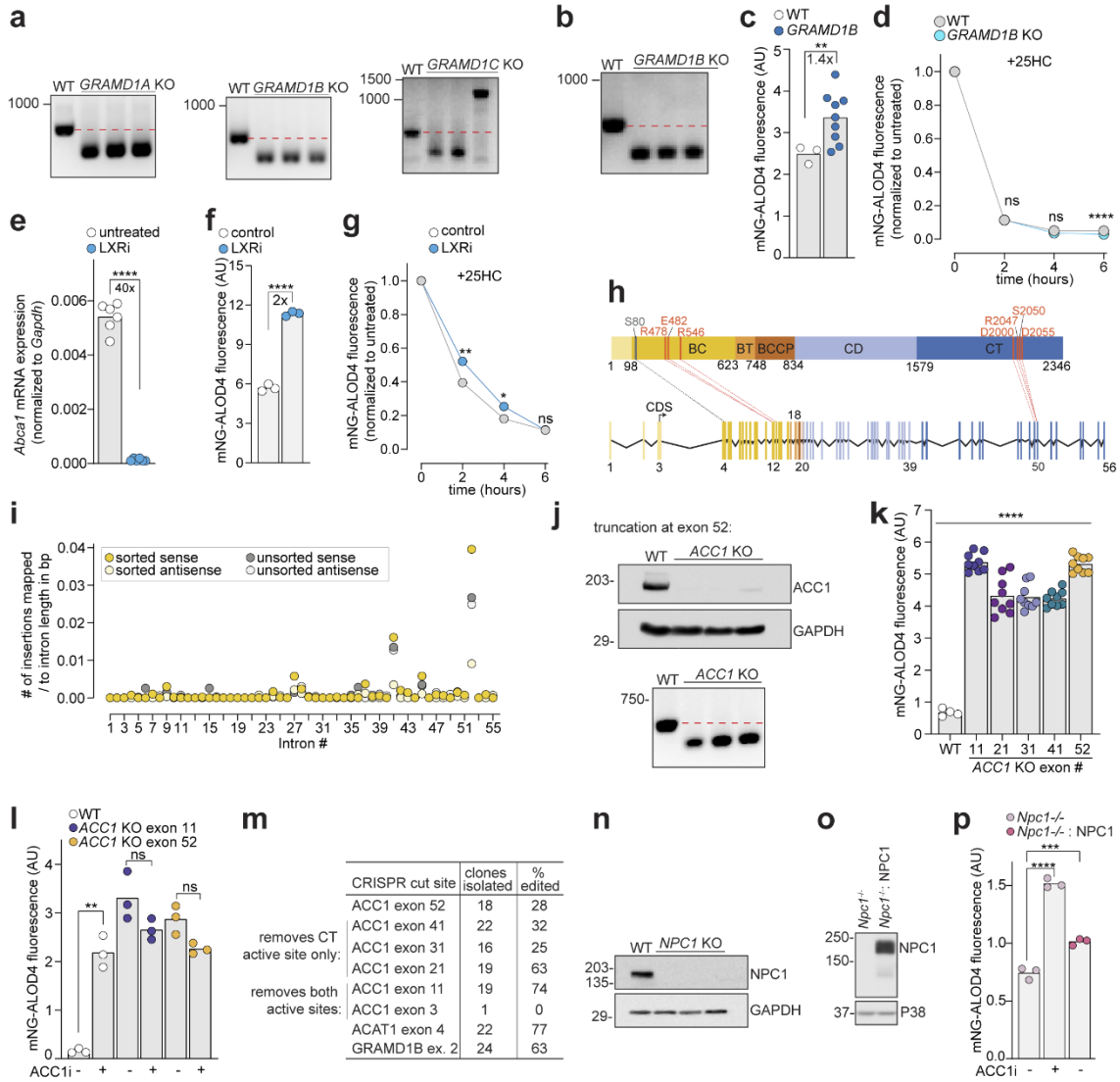

	CRISPR cut site	clones isolated	% edited
	ACC1 exon 52	18	28
removes CT active site only:	ACC1 exon 41	22	32
	ACC1 exon 31	16	25
	ACC1 exon 21	19	63
removes both active sites:	ACC1 exon 11	19	74
	ACC1 exon 3	1	0
	ACAT1 exon 4	22	77
	GRAMD1B ex. 2	24	63

a,**b**, PCR analysis of *GRAMD1A/B/C* TKO clones (**a**) and *GRAMD1B* KO clones (**b**). **c**,**d**, Plasma membrane (PM) cholesterol analyzed by mNG-ALOD4 staining followed by flow cytometry in wild-type (WT) HAP1 and *GRAMD1B* KO clones either left untreated (**c**) or treated with 25HC for the indicated times (**d**). **e**, quantitative real-time PCR analysis of *Abca1* mRNA levels normalized to *Gapdh* levels from 3T3 cells treated for 20 hrs with LXRi (1 μM GSK2033). **f**,**g**, PM cholesterol analyzed by flow cytometry analysis of mNG-ALOD4 staining in 3T3 cells treated for 20 hrs with or without 1 μM of LXRi alone (**f**) or followed by treatment with 25-hydroxycholesterol (25HC) for the indicated times (**g**). **h**, Domain architecture of ACC1 (top) including the biotin carboxylase domain (BC), biotin transferase domain (BT), biotin carboxyl carrier protein domain (BCCP), central domain (CD), and the carboxyltransferase domain (CT) [90,91]. Residues implicated in catalysis are shown in dark orange. Exon map of ACC1 (bottom) with exon colors matching the domain they encode. **i**, The number of insertions mapped per intron are normalized to intron length in base pairs (bp). **j**, Western blot (top) and PCR analysis (bottom) of WT HAP1 and *ACC1* KO clonal cell lines. **k**,**l**, mNG-ALOD4 flow cytometry analysis of PM cholesterol in WT HAP1 and *ACC1* KO cells made with CRISPR sgRNAs targeting the indicated exons either left untreated (**k**) or treated with 30 μM ACC1i (Firsocostat) for 20 hrs (**l**). **m**, Table showing the number of clones isolated from two 96-well dishes and the percentage of those clones that were found to be knockouts with PCR analysis. **n**, Western blot analysis of WT and *NPC1* KO HAP1 cell lines. **o**,**p**, Western blot analysis (**o**) or mNG-ALOD4 flow cytometry analysis of PM cholesterol (**p**) of *Npc1*$^{-/-}$ mouse embryonic fibroblasts (MEFs) or *Npc1*$^{-/-}$ MEFs with NPC1 stably re-introduced using MSCV retrovirus, and then treated with or without ACC1i (30 μM Firsocostat) for 20 hrs. Each data point is the average of three biological replicates (**d** and **g**). Cells in **k** and **l** were grown in 5% lipoprotein depleted serum for 16 hours prior to analysis. Statistical significance was determined by a Student's t-test with a Welch's correction (**c**-**g** and **l**) or an Ordinary one-way ANOVA (**k** and **p**). Exact *p*-values: **c**, WT vs *GRAMD1B* KO p=0.0043; **d**, WT vs *GRAMD1B* KO (2 hr 25HC) p=0.9961, WT vs *GRAMD1B* KO (4 hr 25HC) p=0.0847, and WT vs *GRAMD1B* KO (6 hr 25HC) p<0.0001; **e**, untreated vs LXRi p<0.0001; **f**, control vs LXRi p<0.0001; **g**, control vs LXRi (2 hr 25HC) p=0.0064, control vs LXRi (4 hr 25HC) p=0.0132 and control vs LXRi (6 hr 25HC) p=0.9640; **k**, WT vs *ACC1* KO exon 11 p<0.0001, WT vs *ACC1* KO exon 21 p<0.0001, WT vs *ACC1* KO exon 31 p<0.0001, WT vs *ACC1* KO exon 41 p<0.0001 and WT vs *ACC1* KO exon 52 p<0.0001; **l**, WT untreated vs ACC1i p=0.0076, *ACC1* KO exon 11 untreated vs ACC1i p=0.1371 and *ACC1* KO exon 52 untreated vs ACC1i p=0.0563; and **p**, *Npc1*$^{-/-}$ untreated vs ACC1i p<0.0001 and *Npc1*$^{-/-}$ *vs* *Npc1*$^{-/-}$:NPC1 p=0.0004.

Extended data Fig. 2

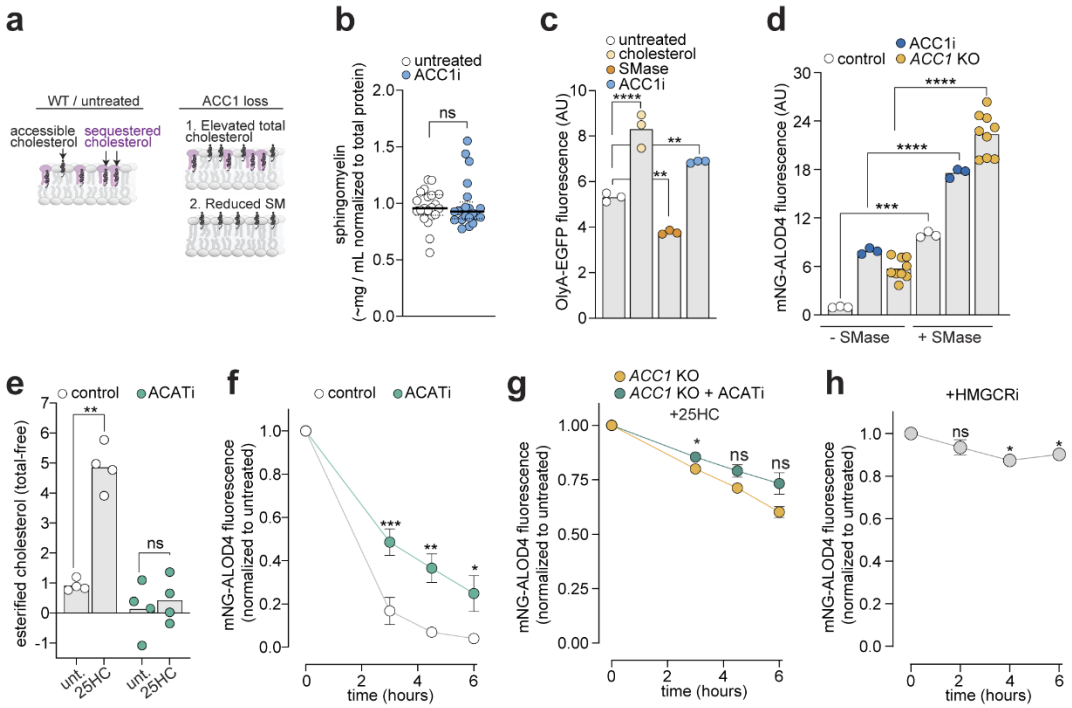

a, Schematic demonstrating that sphingomyelin (SM, purple) binds to cholesterol in membranes. ACC1 loss could elevate cholesterol by 1) increasing cholesterol or by 2) reducing SM levels. **b**, Mass spectrometry analysis of SM levels in wild-type (WT) HAP1 cells either left untreated or treated with ACC1i (30 μM Firsocostat) for 16 hrs. **c**, OlyA-EGFP flow cytometry analysis of WT HAP1 cells left untreated or treated with 0.3 mM MβCD: cholesterol or 150 mU/mg SMase for 30 minutes, or 30 μM ACC1i for 16 hrs. **d**, *ACC1* KO cells or WT HAP1 cells were left untreated or treated for 16 hrs with 30 μM ACC1i. Cells were then treated with or without 150 mU/mg SMase in 5% FBS for 30 minutes and stained with mNG-ALOD4 and analyzed by flow cytometry. **e**, Quantification of esterified cholesterol in WT HAP1 cells treated with ACATi (60 μM SZ58-035) for 16 hrs or left untreated, followed by a 6 hr treatment with or without 4 μM 25HC using the Amplex Red assay. **f**, Flow cytometry analysis of mNG-ALOD4 staining in WT HAP1 cells treated with or without 60 μM ACATi for 16 hrs, followed by 4 μM 25HC for the times indicated. **g**, **h**, mNG-ALOD4 flow cytometry analysis of *ACC1* KO cells left untreated or treated for 16 hours with ACATi (60 μM SZ58-035) followed by 4 μM 25HC treatment for the indicated times (**g**) and WT HAP1 cells grown in 5% FBS and treated with HMGCRi (10 μM Lovastatin) for the indicated times (**h**). Statistical significance was determined by a Student's t-test with a Welch's correction (**b** and **d**-**g**) or an Ordinary one-way ANOVA (**c** and **h**). Exact *p*-values: **b**, untreated vs ACC1i $p=0.6634$; **c**, untreated vs cholesterol $p<0.0001$, untreated vs SMase $p=0.0038$, untreated vs ACC1i $p=0.0036$; **d**, control with vs without SMase $p=0.0002$, ACC1i with vs without SMase $p<0.0001$, *ACC1* KO with vs without SMase $p<0.0001$; **e**, control untreated vs 25HC $p=0.0013$ and ACATi vs ACATi + 25HC $p=0.6469$; **f**, control vs ACATi (3 hr 25HC) $p=0.0004$, control vs ACATi (4.5 hr 25HC) $p=0.0024$ and control vs ACATi (6 hr 25HC) $p=0.0146$; **g**, *ACC1* KO vs *ACC1* KO + ACATi (3 hr 25HC) $p=0.0134$, *ACC1* KO vs *ACC1* KO + ACATi (4.5 hr 25HC) $p=0.0654$ and *ACC1* KO vs *ACC1* KO + ACATi (6 hr 25HC) $p=0.0735$; **h**, 0 vs 2 hrs HMGCRi $p=0.2028$, 0 vs 4 hrs HMGCRi $p=0.0137$ and 0 vs 6 hrs HMGCRi $p=0.0495$.

Extended data Fig. 3

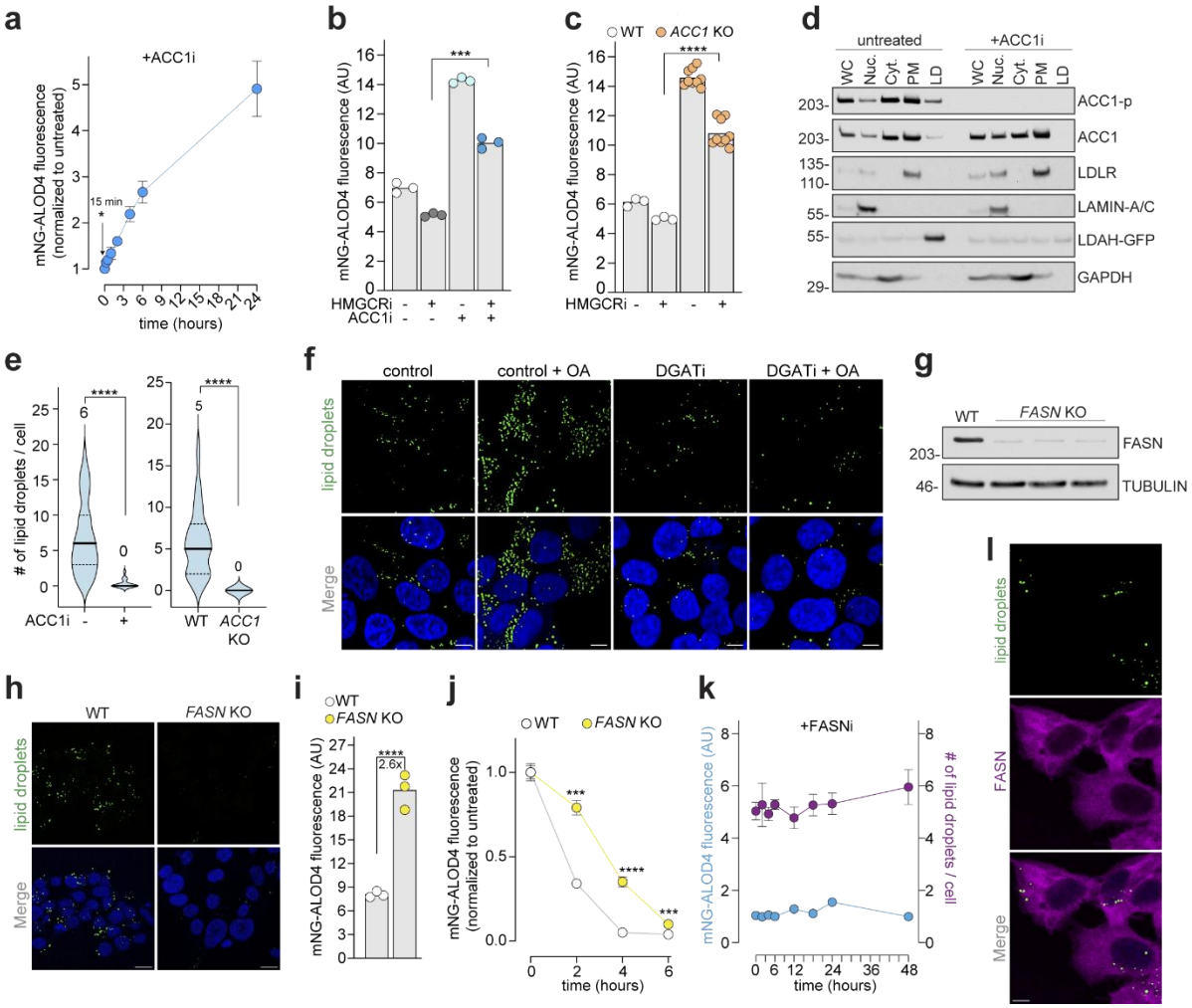

a, 3T3 cells were treated with 30 μM ACC1i (Firsocostat) for the indicated times in 5% FBS, then analyzed by flow cytometry after staining with mNG-ALOD4. **b**, mNG-ALOD4 flow cytometry analysis of WT HAP1 cells cultured in 5% FBS and either left untreated or treated with HMGCRi (10 μM Lovastatin), ACC1i (30 μM Firsocostat) or both for 16 hrs. **c**, mNG-ALOD4 flow cytometry analysis of WT HAP1 cells and *ACC1* KO cells grown in 5% FBS and either left untreated or treated with HMGCRi (10 μM Lovastatin) for 16 hrs. **d**, Western blot analysis of fractionated LDAH-GFP expressing HAP1 cells with various cellular fractions including whole cell (WC), nucleus (Nuc.; detected by LaminA/C), cytoplasm (Cyt.; detected by GAPDH), plasma membrane (PM; detected by LDLR), and lipid droplets (LD; detected by LDAH-GFP). Cells were either left untreated or treated with ACC1i (30 μM Firsocostat) for 24 hrs. **e**, Quantification of LD numbers per cell in WT HAP1 cells treated with or without ACC1i (30 μM Firsocostat) for 16 hrs (left) or WT HAP1 cells compared to *ACC1* KO HAP1 cells (right). The solid middle line shows the median and dashed lines show the interquartile range. **f**, Microscopy images of LDs in WT HAP1 cells left untreated or treated with DGAT1 and DGAT2 inhibitors (DGATi) for 16 hrs followed by 150 μM oleic acid (OA) treatment for 6 hrs in 5% FBS stained with Bodipy 493/503. Scale bar is 10 microns. **g**, Western blot analysis of WT HAP1 cells compared to *FASN* KO HAP1 clones. **h**, Microscopy images of LDs in WT HAP1 and *FASN* KO cells stained with Bodipy 493/503 and DAPI (blue). Scale bar is 10 microns. **i**,**j**, Flow cytometry analysis of mNG-ALOD4 PM staining in WT HAP1 and *FASN* KO clones grown in 5% LDS media for 24 hrs left untreated (**i**) or then treated with 4 μM 25HC for the indicated times (**j**). **k**, mNG-ALOD4 flow cytometry analysis of PM accessible cholesterol (blue curves) and the corresponding fluorescence microscopy quantification of the number of LDs per cell (purple curves) in HAP1 cells grown in 5% FBS and then treated with FASNi (10 μM C75) for the indicated times in 5% LDS. LDs were quantified by taking the mean number of LDs per cell in four fields of view with ~75 cells per field. **l**, Microscopy images of FASN localization relative to LD staining with Bodipy 493:503. Scale bar is 5 microns. Statistical significance was determined by a Student's t-test with a Welch's correction (**a-c,e,i** and **j**). Exact *p*-values: **a,** 0 vs 15 min ACC1i p=0.0419; **b,** WT HMGCRi vs HMGCRi + ACC1i p=0.0008 ; **c,** WT HMGCRi vs *ACC1* KO HMGCRi p<0.0001; **e,** WT untreated vs ACC1i p<0.0001 and WT vs *ACC1* KO p<0.0001; **i,** WT vs *FASN* KO p<0.0001; **j,** WT vs *FASN* KO (2 hr 25HC) p=0.0001, WT vs *FASN* KO (4 hr 25HC) p<0.0001 and WT vs *FASN* KO (6 hr 25HC) p=0.0003.

Extended data Fig. 4

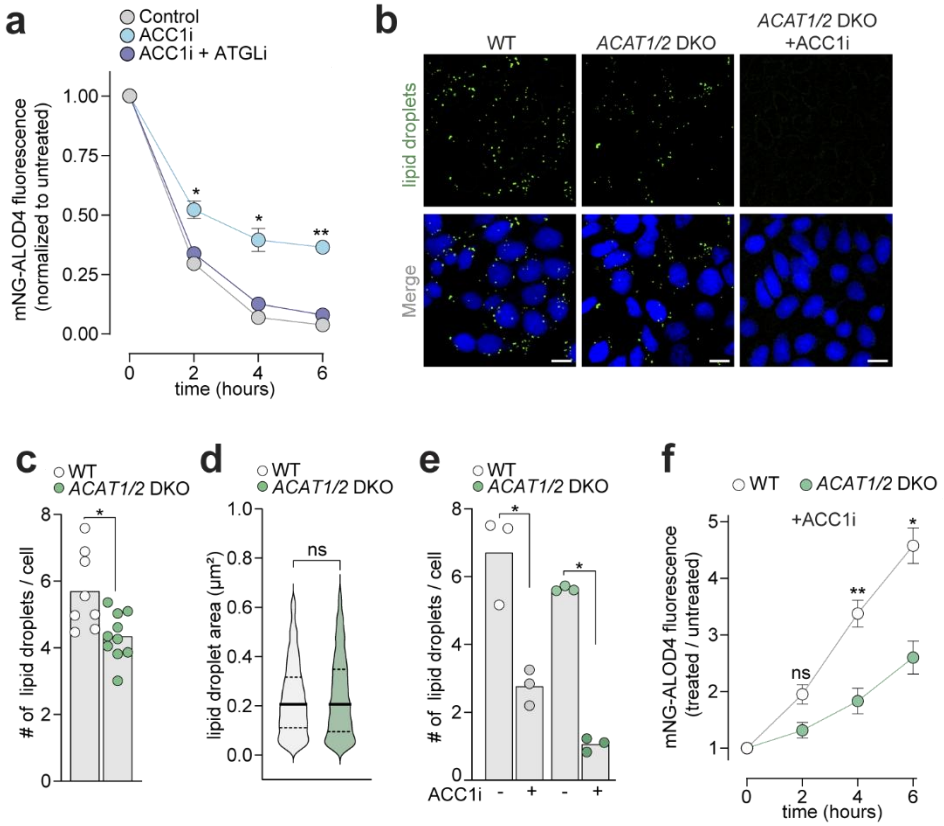

a, Flow cytometry analysis of PM mNG-ALOD4 staining. WT HAP1 cells were left untreated, treated with ACC1i (30 µM Firsocostat), or treated with both ACC1i and ATGLi (50 µM NG-497), followed by treatments with 4 µM 25HC for the indicated times. **b**, Microscopy images of LDs in WT HAP1, untreated *ACAT1/2* DKO and *ACAT1/2* DKO treated with ACC1i (30 µM Firsocostat) and stained with Bodipy 493/503 and DAPI (blue). Scale bar is 10 microns. **c**, Quantification of LD numbers per cell in WT and *ACAT1/2* DKO HAP1 cells cultured in 5% LDS for 24 hrs. **d**, LD area for untreated WT and *ACAT1/2* DKO HAP1 cells. Each violin plot shows the area for LDs measured in three fields of view. **e**, LD quantification for WT and *ACAT* DKO cells, either untreated or treated with ACC1i (30 µM Firsocostat) for 6 hrs. Each data point is the total number of LDs per cell in one field of view. **f**, Flow cytometry analysis of mNG-ALOD4 staining in WT and *ACAT1/2* DKO HAP1 cell lines cultured in 5% LDS for 16 hrs, followed by treatment with ACC1i (30 µM Firsocostat) for the indicated times. Statistical significance was determined by Student's t-test with Welch's correction (**a** and **c-f**). Exact *p*-values: **a,** WT ACC1i vs ACC1i + ATGLi (2 hr 25HC) *p*=0.0196, WT ACC1i vs ACC1i + ATGLi (4 hr 25HC) *p*=0.0256, and WT ACC1i vs ACC1i + ATGLi (2 hr 25HC) *p*=0.0017; **c**, WT vs *ACAT 1/2* DKO *p*=0.0151; **d**, WT vs *ACAT 1/2* DKO *p*=0.0588; **e**, WT untreated vs ACC1i *p*=0.0186 and *ACAT 1/2* DKO untreated vs ACC1i *p*=0.0146; **f**, WT vs *ACAT1/2* DKO (2 hr ACC1i) *p*=0.1519, WT vs *ACAT1/2* DKO (4 hr ACC1i) *p*=0.0099 and WT vs *ACAT1/2* DKO (6 hr ACC1i) *p*=0.0160.

Extended data Fig. 5

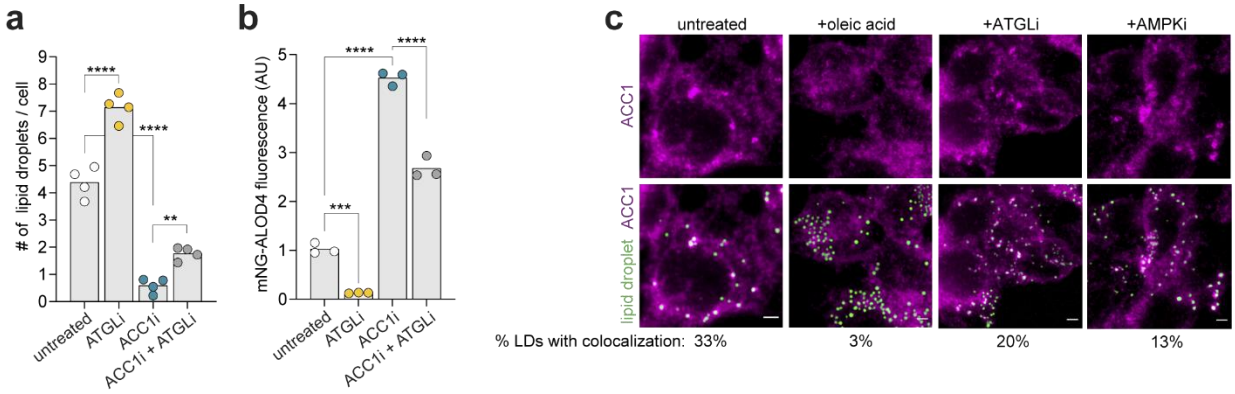

a,**b**, Quantification of lipid droplet (LD) numbers per cell (**a**) or flow cytometry analysis of PM mNG-ALOD4 staining (**b**) in WT HAP1 cells left untreated, treated with ATGLi (50 μM NG-497), ACC1i (30 μM Firsocostat), or both for 16 hrs. **c**, Microscopy images of ACC1 localization relative to LD staining (Bodipy 493:503) in cells treated with 100 μM oleic acid for 6 hrs, ATGLi (50 μM NG-497) for 16 hrs, or AMPKi (2.5 μM Dorsomorphin) for 16 hrs. The percentage of LDs with ACC1 co-localization was determined by dividing the number of LDs with adjacent ACC1 puncta by the total number of LDs. n>250 LDs for all conditions. Scale bar is 5 microns. Statistical significance was determined by an Ordinary one-way ANOVA (**a** and **b**). Exact *p*-values: **a**, untreated vs ATGLi $p<0.0001$, untreated vs ACC1i $p<0.0001$ and ACC1i vs ACC1i + ATGLi $p=0.0058$; and **b**, untreated vs ATGLi $p=0.0002$, untreated vs ACC1i $p<0.0001$ and ACC1i vs ACC1i + ATGLi $p<0.0001$.

Extended data Fig. 6

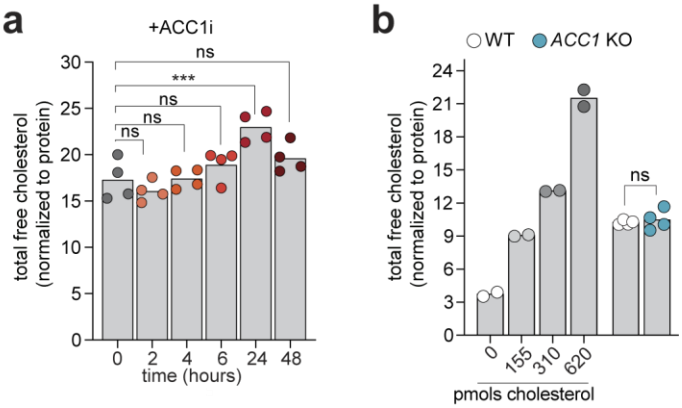

a, Quantification of free (unesterified) cholesterol normalized to total protein in WT HAP1 cells treated with ACC1i (30 μM Firsocostat) for the indicated times using the Amplex Red assay. **b**, Quantification of free (unesterified) cholesterol in WT HAP1 cells and *ACC1* KO cells using the Amplex Red assay. Statistical significance was determined by an Ordinary one-way ANOVA (**a**) or a Student's t-test with a Welch's correction (**b**). Exact *p*-values: **a**, untreated vs 2 hrs ACC1i $p=0.8245$, untreated vs 4 hrs ACC1i $p>0.9999$, untreated vs 6 hrs ACC1i $p=0.5931$, untreated vs 24 hrs ACC1i $p=0.0004$, untreated vs 48 hrs ACC1i $p=0.2352$ and **b**, WT vs *ACC1* KO $p=0.6323$.